

Structural and Lattice-Dynamical Properties of Tb_2O_3 under Compression: A Comparative Study with Rare Earth and Related Sesquioxides

Jordi Ibáñez, Juan Ángel Sans, Vanesa Cuenca-Gotor, Robert Oliva,* Óscar Gomis, Plácida Rodríguez-Hernández, Alfonso Muñoz, Ulises Rodríguez-Mendoza, Matías Velázquez, Philippe Veber, Catalin Popescu, and Francisco Javier Manjón*

Cite This: *Inorg. Chem.* 2020, 59, 9648–9666

Read Online

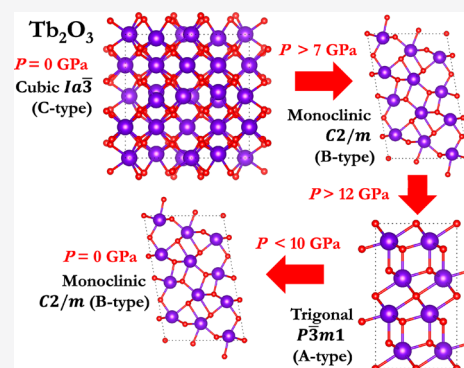
ACCESS |

Metrics & More

Article Recommendations

Supporting Information

ABSTRACT: We report a joint experimental and theoretical investigation of the high pressure structural and vibrational properties of terbium sesquioxide (Tb_2O_3). Powder X-ray diffraction and Raman scattering measurements show that cubic $Ia\bar{3}$ (C-type) Tb_2O_3 undergoes two phase transitions up to 25 GPa. We observe a first irreversible reconstructive transition to the monoclinic $C2/m$ (B-type) phase at ~ 7 GPa and a subsequent reversible displacive transition from the monoclinic to the trigonal $P\bar{3}m1$ (A-type) phase at ~ 12 GPa. Thus, Tb_2O_3 is found to follow the well-known $C \rightarrow B \rightarrow A$ phase transition sequence found in other cubic rare earth sesquioxides with cations of larger atomic mass than Tb. Our *ab initio* theoretical calculations predict phase transition pressures and bulk moduli for the three phases in rather good agreement with experimental results. Moreover, Raman-active modes of the three phases have been monitored as a function of pressure, while lattice-dynamics calculations have allowed us to confirm the assignment of the experimental phonon modes in the C- and A-type phases as well as to make a tentative assignment of the symmetry of most vibrational modes in the B-type phase. Finally, we extract the bulk moduli and the Raman-active mode frequencies together with their pressure coefficients for the three phases of Tb_2O_3 . These results are thoroughly compared and discussed in relation to those reported for rare earth and other related sesquioxides as well as with new calculations for selected sesquioxides. It is concluded that the evolution of the volume and bulk modulus of all the three phases of these technologically relevant compounds exhibit a nearly linear trend with respect to the third power of the ionic radii of the cations and that the values of the bulk moduli for the three phases depend on the filling of the f orbitals.



1. INTRODUCTION

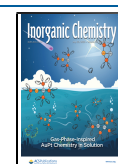
Rare earth (RE) sesquioxides (SOs), in particular lanthanide SOs (Ln_2O_3 ; $Ln = La$ to Lu , Y , and Sc), are an important family of materials due to their remarkable fundamental properties and potential applications. These compounds are highly interesting and versatile for different types of applications because the Ln radius can be finely tuned along the lanthanide family with the filling of f orbitals, thus enabling a wide range of technological advances including light emitters (lasers and improved phosphors), catalysts, and high-dielectric constant (high-k) gates. In particular, terbium sesquioxide (Tb_2O_3) has attracted considerable attention in the past few years as a high-k material^{1–3} and also as an active material for optical insulators and high-performance optoelectronic devices.^{4–6}

It is well-known that RE SOs exhibit three polymorphic modifications at room conditions, depending on the RE radius: (i) a trigonal phase, named A-type (space group (s.g.) $P\bar{3}m1$, No. 164, $Z = 1$), for large cations from La to Nd ; (ii) a

monoclinic phase, named B-type (s.g. $C2/m$, No. 12, $Z = 6$), for medium-size cations from Sm to Gd ; (iii) a cubic bixbyite-type phase, named C-type (s.g. $Ia\bar{3}$ No. 206, $Z = 16$), for small cations from Tb to Lu , including Y and Sc . The bixbyite phase also occurs at ambient pressure in other SOs, like Mn_2O_3 , In_2O_3 , and Tl_2O_3 . At high temperatures, two additional phases named as H (hexagonal, s.g. $P6_3/mmc$, No. 194, $Z = 2$) and X (cubic, s.g. $Im\bar{3}m$, No. 229, $Z = 4$) have also been found in RE SOs.⁷ Phase transitions (PTs) of Ln_2O_3 at high temperatures have been summarized by Zinkevich,⁸ and many of them usually follow the sequence $C \rightarrow B \rightarrow A$ when increasing temperature. In particular, Tb_2O_3 was observed to undergo the

Received: March 19, 2020

Published: June 25, 2020



C → B PT above 1600–1875 °C,^{7,9,10} followed by the B → H PT above 2430–2450 °C^{7,11,12} and the H → X PT above 2610–2640 °C.^{11,12}

Since the molar volume (density) of the A-, B-, and C-type phases decreases (increases) in the order C, B, and A, the PT sequence C → B → A is expected for most RE SOs crystallizing in the cubic phase, either at high pressure (HP) or at high temperature (HT).^{13,14} The effect of HP on RE SOs has been extensively studied by several research groups, and their pressure-induced PTs have been recently reviewed.¹⁵ In fact, since the cubic phase can be synthesized in a number of them, from Lu to Sm as well as in Mn₂O₃, In₂O₃, and Tl₂O₃, its behavior under compression has been widely studied, as for instance in Lu₂O₃,^{16,17} Yb₂O₃,^{18,19} Tm₂O₃,^{20,21} Er₂O₃,^{22–24} Ho₂O₃,^{25–28} Dy₂O₃,^{29,30} Gd₂O₃,^{31–38} Eu₂O₃,^{39–45} Sm₂O₃,^{34,46,47} Sc₂O₃,^{48–50} Y₂O₃,^{34,51–61} Mn₂O₃,^{62–65} In₂O₃,^{66–70} and Tl₂O₃.⁷¹ Moreover, the equation of state of several RE SOs of C-, B-, and A-type has been studied comparatively.⁷²

Polymorphism of RE SOs and their transformations at HP have also been investigated theoretically, and the simulations of the bandgap, volume, bulk modulus, and its pressure derivative for the C-, B-, and A-type phases as well as their PT pressures have been reported and found in rather good agreement with experiments.^{73–85} In fact, several theoretical works have reported the study of the bulk modulus of C-type RE SOs as a function of the atomic number,^{84,86} however, the overall behavior of the bulk modulus as a function of unit-cell volume and cation radius remains to be investigated for all three C-, B-, and A-type phases. Besides, the explanation of the behavior of the bulk modulus as a function of the unit-cell volume for all C-type SOs, including not only Ln₂O₃ but also bixbyite-type SOs, such as Sc₂O₃, Mn₂O₃, Y₂O₃, In₂O₃, and Tl₂O₃, is still awaiting. Moreover, there is no idea about the ordering of the values of bulk moduli in the three phases.

Despite the large amount of work performed on the study of Ln₂O₃ properties at HP, relatively little is known about Tb₂O₃ under compression. Hoekstra and Gingerich transformed the cubic phase into the monoclinic one at 2.5 GPa and 905 °C.¹³ However, no experimental data are available, up to our knowledge, for A-type Tb₂O₃ to compare with theoretical estimations.^{76,79,84,86} The lack of studies on Tb₂O₃ lies in the difficulty of synthesizing this material that usually crystallizes at room conditions in the C-type structure. The reason for the difficult synthesis of Tb₂O₃ is the tendency of terbium oxide to grow naturally as Tb₄O₇, a mixed valence compound with Tb atoms in both 3+ and 4+ valence states.^{75,87} Fortunately, it has been recently shown that pure millimeter-sized C-type Tb₂O₃ single crystals can be grown via a controlled atmosphere flux method.⁸⁸ The high quality cubic Tb₂O₃ crystals thus obtained are highly promising for applications in optics and photonics. Using such high quality material, the room-pressure lattice-dynamics properties of cubic Tb₂O₃ have been recently investigated.⁸⁹

In the last two decades, a vast number of HP studies have been devoted to investigate the behavior of RE SOs under compression. Although the pressure-induced PT sequence has been well established, the structural and vibrational properties of most of these compounds under compression, i.e., the equation of state (bulk moduli) and vibrational properties, are not so well understood and show little consistency across the investigated literature. Therefore, a more consistent work from both experimental and theoretical points of view is required to

achieve a better understanding of the structural and vibrational properties of RE SOs.

In this work, we present a thorough experimental and theoretical study on the structural and vibrational properties of Tb₂O₃ under compression, where powder X-ray diffraction (XRD) and Raman scattering (RS) measurements at HP have been complemented with theoretical *ab initio* calculations. We will show that C-type Tb₂O₃ undergoes two PTs up to 25 GPa: a first irreversible C → B PT and a second reversible B → A PT. The experimental and theoretical equation of state (EoS) of the three phases of Tb₂O₃ will be provided and compared with those of isostructural compounds. In particular, we will show that there is a linear trend between the bulk moduli of the three C-, B-, and A-type phases and the cube cation ionic radius and that the ordering of the bulk moduli for each phase depends on the filling of the f levels. Additionally, up to 13 optical Raman-active modes of C-type Tb₂O₃ have been monitored as a function of pressure, while 16 and 4 Raman-active modes have been observed in the B- and A-type phases, respectively. The assignment of the symmetries of the different phonons in the three phases is supported by the results of *ab initio* lattice-dynamics calculations, and the experimental and theoretical phonon pressure coefficients in the three phases have been compared with those of isostructural SOs, with a special emphasis in the less known A-type SOs.

2. EXPERIMENTAL METHODS

Millimeter-sized pure cubic Tb₂O₃ single crystals with [112] crystallographic orientation were the starting material employed in this study.⁸⁸ Details of the growth method and the structural and vibrational properties of the Tb₂O₃ single crystals at room conditions can be found elsewhere.^{88,89} The single crystals were ground for powder XRD experiments, which were first performed at room conditions with a PANalytical X'Pert Pro MPD diffractometer (Cu K α 1 K α 2 radiation). Le Bail fits confirmed the cubic *Ia* $\bar{3}$ symmetry and allowed one to extract a lattice parameter, $a = 10.7323(3)$ Å, and volume, $V = 1236.17$ Å³, in good agreement with previous structural characterizations.^{10,90} No reflections arising from the Li₆Tb(BO₃)₃ solvent employed during growth, or from other impurity phases, were detected in the XRD scans.

Powder angle-dispersive XRD measurements at HP were performed at room temperature in the BL04-MSPD beamline at ALBA synchrotron facility.⁹¹ This beamline is equipped with Kirkpatrick-Baez mirrors to focus the monochromatic beam and a Rayonix CCD detector with a 165 mm diameter active area. The XRD measurements were performed with monochromatic X-rays with a wavelength of 0.4246 Å, as determined from the absorption K-edge of Sn (29.2 keV). The sample was loaded with a 4:1 methanol–ethanol mixture in a membrane-type diamond anvil cell (DAC) with diamond culets of 400 μ m in diameter. The applied pressure was determined with the EoS of copper.⁹² The associate error to the pressure determination, including the pressure gradients inside the DAC, is lower than 0.2 GPa. The sample to detector distance (240 mm), along with various detector geometrical parameters of the experiment, were calibrated with the DIOPTAS software⁹³ using diffraction data from LaB₆ measured in the same conditions as the sample. The structural analyses were performed with the program TOPAS 4.2. For the low pressure (LP) cubic phase, Rietveld refinements to the XRD patterns were carried out, whereas for the HP phases, the lattice parameters were obtained with Pawley/Le Bail whole pattern fittings. Figure S1 shows selected examples of calculated and difference profiles as obtained from the profile refinements.

Room-temperature unpolarized HP-RS measurements were excited with the 532 nm line of a solid state laser. For these experiments, micronsize fragments without well-known orientation were obtained from the single crystals. Inelastically scattered light was collected with a Horiba Jobin Yvon LabRAM HR UV spectrometer equipped with

an edge filter that cuts Raman signals below ~ 50 cm^{-1} and a thermoelectrically cooled multichannel CCD detector enabling a spectral resolution better than 2 cm^{-1} . The applied pressure was determined using the luminescence of small ruby chips evenly distributed in the pressure chamber.⁹⁴ Phonon signals were analyzed by fitting the Raman peaks with a pseudo-Voigt profile.

3. FIRST-PRINCIPLES CALCULATIONS

Ab initio total-energy calculations at 0 K for the C-, B-, and A-type phases of Tb_2O_3 (and also for other SOs) were performed within the framework of density functional theory (DFT)⁹⁵ with the Vienna Ab-initio Simulation Package (VASP),⁹⁶ using the pseudopotential method and the projector augmented waves (PAW) scheme.^{97,98} In this work, the generalized gradient approximation (GGA) with the Perdew–Burke–Ernzerhof (PBE) parametrization⁹⁹ was used for the exchange and correlation energy, after evaluating the calculations performed also with its extension to the solid state (PBEsol).¹⁰⁰ A dense Monkhorst–Pack grid¹⁰¹ of special k -points ($6 \times 6 \times 6$ for the C phase and $4 \times 4 \times 4$ for the A and B phases) and a plane-wave basis set with energy cutoffs of 530 eV were used. Lattice-dynamical properties were obtained for the Γ -point using the direct-force constant approach¹⁰² with both PBE and PBEsol functionals in order to compute the atomic forces. A comparison of data with both GGA-PBE and GGA-PBEsol prescriptions led us to use, in most cases, the GGA-PBE data for the joint analysis with the experimental results, unless otherwise specified.

4. RESULTS AND DISCUSSION

4.1. Structural Properties of Tb_2O_3 under Pressure.

Tb_2O_3 crystallizes in the cubic C-type polymorph (or bixbyite-type), a structure traditionally understood as derived from the fluorite lattice by doubling the lattice parameter and leaving one-fourth of the anion sites vacant in an ordered way (see Figure 1). In fact, the bixbyite structure is an intermediate

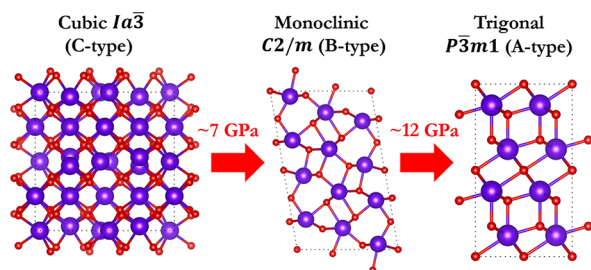


Figure 1. Crystal structure of the C-, B-, and A-type phases of Tb_2O_3 . Structural PTs take place at ~ 7 GPa (C \rightarrow B) and ~ 12 GPa (B \rightarrow A).

structure between the zincblende and the fluorite structure, since the cation array, which derives from the face-centered cubic structure present in Ln atoms at ambient conditions, is the same in the three structures.^{103,104}

In C-type Tb_2O_3 , there are three independent atoms, Tb1, Tb2, and O. Tb1 and Tb2 atoms are located at 8b and 24d Wyckoff sites, respectively, while O atoms occupy 48e sites. Therefore, this structure has only 4 free atomic coordinates, the x_{Tb} parameter of the Tb2 atom, usually denoted as u , and the three atomic coordinates (x_{O} , y_{O} , z_{O}) of the O atom. In this structure, O atoms show 4-fold coordination, and both Tb atoms show 6-fold coordination. The differences in bonding found for the two different Ln atoms of the C-type structure

have been previously discussed.¹⁰⁵ In particular, O atoms around Tb1 form a regular octahedron with 6 equal Tb–O distances around 2.285 Å, while O atoms around Tb2 form an irregular octahedron with three different Tb–O distances around 2.274, 2.297, and 2.391 Å. The different environment of the two inequivalent Tb sites can be understood if one considers that the C-type structure derives from the fluorite lattice, where two O atoms out of the eight O atoms surrounding Tb atoms in a cube are removed along (111) and (110) directions.⁸⁰ This gives rise to two different configurations for Tb atoms, with the first configuration being more regular than the second one.

Figure 2 shows the HP-XRD patterns of Tb_2O_3 at room temperature for selected pressures up to 20 GPa. It can be

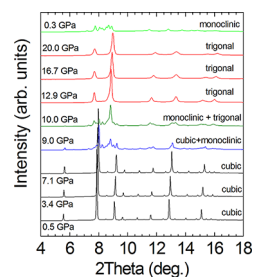


Figure 2. Room-temperature HP-XRD patterns of Tb_2O_3 at selected pressures up to 20 GPa. The top scan shows the resulting pattern at 0.3 GPa after pressure release in the downstroke.

observed that all the scans from 0 to ~ 7 GPa are dominated by peaks of the C-type phase. However, new reflections, which start to be visible at 7.1 GPa (not seen in Figure 2 due to scaling reasons) and are observed up to 11.2 GPa, can be indexed with the B-type phase. On the upstroke, the B-type phase was always found to be accompanied by the C-type or the A-type phase, this last phase emerging around 12.0 GPa. Above this pressure, the A-type peaks start to broaden upon compression, most probably as a consequence of the loss of hydrostatic conditions of the pressure-transmitting medium.¹⁰⁶ The experimental values of 7.1 and 12.0 GPa for the C \rightarrow B and B \rightarrow A PTs, respectively, are in good agreement with those predicted by our calculations using GGA-PBE DFT calculations, which locate both PTs around 5.5 and 10.9 GPa, respectively (see Figure 3). These values are also in good

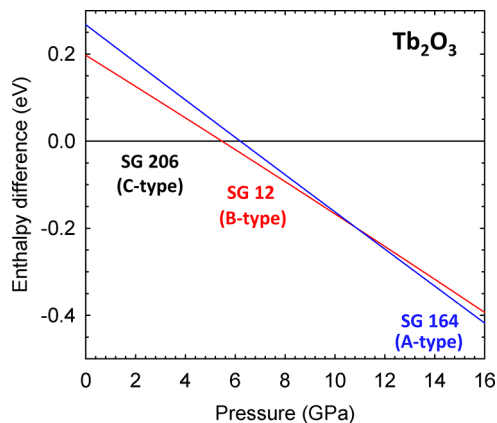


Figure 3. Enthalpy difference between the B-type (red line) and A-type (blue line) phases of Tb_2O_3 with respect to the C-type (black line) phase as a function of pressure.

agreement with the PT pressures reported in other RE SOs.¹⁵ The XRD peaks of the A-type phase show up in the scans up to the maximum pressure of the experiment (20 GPa). Although these reflections could also be indexed with the H-type phase, RS measurements (see below) confirm that the phase above 12.0 GPa corresponds to the A-type structure. On the downstroke, this phase was found to back-transit to the B-type phase around 10 GPa, with this latter phase being metastably observed down to room pressure (see the top XRD scan in Figure 2). In fact, the volume and lattice parameters obtained for the B-type phase at room pressure (see Tables 1 and 2) agree nicely with those previously reported.^{10,107,108}

Table 1. EoS Parameters of the Cubic (C), Monoclinic (B), and Trigonal (A) Phases of Tb₂O₃ Obtained from Fits to the Experimental (exp) and DFT-PBE Theoretical (the) Data Obtained in This Work^a

phase	V ₀ (Å ³)	B ₀ (GPa)	B ₀ '	EoS
C (exp)	77.3(1)	148(2)	2.1(4)	BM3
C (the)	77.5(1)	140.5(4)	4.2(1)	BM3
B (exp)	71.0(1)	133(3)	4 (fixed)	BM2
B (the)	71.5(2)	135.3(6)	4 (fixed)	BM2
A (exp)	71.0(6)	112(5)	4 (fixed)	BM2
A (the)	70.3(1)	133.9(2)	4 (fixed)	BM2

^aThe last column indicates the type of EoS employed to fit the data. Volumes are given per formula unit.

The experimental pressure dependence of the unit-cell volume of the different phases of Tb₂O₃ up to 20 GPa, as obtained from Rietveld analysis, is plotted in Figure 4. For comparison purposes, all the data in this figure correspond to the unit-cell volume per formula unit (pfu). Theoretical data are also plotted in Figure 4 with solid lines for direct comparison with the experimental results. A fit of pressure vs experimental unit-cell volume to a third-order Birch–Murnaghan (BM) EoS¹¹⁰ yields, for the case of C-type Tb₂O₃ (*Z* = 16), a zero-pressure unit-cell volume, V₀, bulk modulus, B₀, and pressure derivative of the bulk modulus, B₀', of V₀ = 1236.2(2) Å³, B₀ = 148(2) GPa, and B₀' = 2.1(4), respectively. The value of V₀ obtained from the third-order BM-EoS fit is similar to that measured outside the DAC and in previous reports.^{10,90} We have also fitted the experimental data with a second-order BM-EoS, which yields V₀ of 1237.0(2) Å³ and a somewhat larger bulk modulus, B₀, of 139(2) GPa (B₀' = 4 in this case). On the other hand, the fit of the theoretical GGA-PBE data using a third-order BM-EoS yields the following values: V₀ = 1240.12(4) Å³, B₀ = 140.5(4) GPa, and B₀' = 4.2(1), respectively. Note that there is an excellent

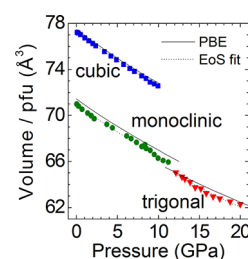


Figure 4. Unit-cell volume per formula unit (pfu) as a function of the applied pressure for the three phases of Tb₂O₃ as obtained experimentally (symbols). Solid (dashed) lines represent the results of the *ab initio* calculations (fits of experimental data). Calculated errors for the experimental values are smaller than the sizes of the symbols in all cases.

agreement between our experimental and theoretical V₀ and B₀ values for C-type Tb₂O₃ (see Table 1). Note also that, despite the experimental B₀ obtained with the second-order EoS being somewhat closer to the theoretical value, here we rely on the result obtained with the third-order EoS because the normalized stress vs Eulerian strain plot (not shown) is slightly better in this case. To conclude, we want to emphasize that our theoretical B₀ for C-type Tb₂O₃ is also in good agreement with some recent theoretical predictions using GGA-PBE calculations^{84,86} (see Tables S1 and S2, which display experimental and theoretical data for different SOs). The theoretical and experimental values of V₀, B₀, and B₀' for the C-type phase, as well as those for the B-type and A-type phases of Tb₂O₃ studied below, are summarized in Table 1, whereas experimental and theoretical data of the lattice parameters for the three phases can be found in Table 2.

The good agreement observed between our theoretical and experimental data for the unit-cell volume of C-type Tb₂O₃ is also found in the evolution of its free atomic coordinates (see Figure S2a) and in the different Tb–O distances as a function of pressure. Results of theoretical calculations and of Rietveld refinement of the experimental data for Tb₂O₃ show that the four free atomic coordinates *x*_{Tb}, *x*_O, *y*_O, and *z*_O exhibit a negligible change between 0 and 10 GPa (Figure S2a). This result implies that there is a monotonous decrease of the Tb–O distance with pressure in the C-type phase (Figure S2b) that is basically determined by the lattice parameter reduction.

We have not found in the literature a report of any pressure dependence of the atomic coordinates or of the cation–anion interatomic distances in other isostructural C-type or bixbyite-type SOs. Our present calculations in Lu₂O₃, Sc₂O₃, and In₂O₃ (see Figure S3) show that their atomic parameters also exhibit a negligible change with pressure irrespective of the HP phase

Table 2. Experimental (exp) and GGA-PBE Theoretical (the) Zero-Pressure Lattice Parameters of the Cubic (C) and Monoclinic (B) Phases of Tb₂O₃^a

	<i>a</i> (Å)		<i>b</i> (Å)		<i>c</i> (Å)		β (deg.)	
	exp.	the.	exp.	the.	exp.	the.	exp.	the.
C-type ^b	10.732(1)	10.743						
	10.730 ^d	10.735 ^e						
B-type ^b	14.005(5)	14.136	3.543(5)	3.535	8.718(5)	8.718	100.1(1)	100.33
	14.04(1) ^c	14.13 ^f	3.541(3) ^c	3.537 ^f	8.725(8) ^c	8.716 ^f	100.06(5) ^c	100.21 ^f
A-type ^b	3.658(5)	3.646			5.610(5)	5.646		
		3.715 ^f				5.858 ^f		

^aThe parameters of the trigonal (A) phase of Tb₂O₃ are given at 12.2 GPa. ^bThis work. ^cRef 107. ^dRef 109. ^eRef 86. ^fRef 79.

acquired by the cubic SO. The negligible change of atomic parameters and the consequent monotonous and parallel decrease of interatomic distances of cubic SOs under hydrostatic compression are very interesting. It means, on one hand, that there is no net increase of the effective coordination number either of the metal atoms or of O atoms with an increase pressure and, on the other hand, that the two low-symmetry Wyckoff positions for metal (24d) and O (48e) atoms in the C-type/bixbyite-type structure behave like very high-symmetry positions, i.e., with all atomic coordinates almost fixed to certain values. This behavior is in contrast to what happens in corundum-type SOs, like In_2O_3 and Al_2O_3 (see Figure S4). As observed, the theoretical free atomic parameters of Al_2O_3 up to 30 GPa show the opposite behavior of those of In_2O_3 . Clearly, the different change of the free atomic parameters of the corundum phase in Al_2O_3 and In_2O_3 at HP explains why InO_6 and AlO_6 octahedra evolve in a different way with pressure, as recently reported, and perhaps why corundum-type Al_2O_3 is more stable than isostructural In_2O_3 at HP.⁷⁰

We have to note that the negligible change of the atomic parameters in C-type SOs at HP is consistent with the negligible variation of those parameters upon changing ionic radius, as noted by Richard et al.⁸³ In this context, it must be recalled that the lanthanide contraction on going from La to Lu, and even to Sc, can be viewed as a chemical pressure similar to physical pressure, so both the effects of pressure and contraction of ionic radius are comparable. Figure S3 shows that the atomic coordinates of nonlanthanide bixbyite-type SOs (In_2O_3 , Tl_2O_3 , Mn_2O_3 , etc.) exhibit exactly the same values as those of C-type RE SOs (including Sc_2O_3 and Y_2O_3), so both types of compounds are isostructural. This adds additional interest to the different pressure-induced PTs observed in these isostructural compounds, since the cubic lanthanide SOs undergo PTs to B- and A-type phases, while cubic nonlanthanide SOs undergo PTs to phases related to the corundum-type structure.

The C \rightarrow B PT occurs in Tb_2O_3 at ~ 7 GPa on the upstroke. This is a first-order PT with an experimental (theoretical) relative volume reduction of 8% (7.8%). The B-type phase, shown in Figure 1, is characterized by having one O atom at a 2b site as well as three Tb atoms and four O atoms at 4i Wyckoff sites. This structure has no fixed atomic coordinates, so the seven inequivalent atoms at the 4i sites contain 21 free coordinates. In particular, B-type Tb_2O_3 has two Tb atoms (Tb1 and Tb2) with 7-fold coordination and one Tb atom (Tb3) with 6-fold coordination. In regard to O atoms, O1 has 5-fold coordination; O2, O3, and O4 have 4-fold coordination, and O5 has 6-fold coordination. Therefore, on average, the coordination of Tb is around 6.5 and that for O is around 4.8. The B-type phase of RE SOs is also characterized by a cationic array that is a distortion of the hexagonal closed packed (hcp) structure of metals ($P6_3/mmc$, No. 194, $Z = 2$). In the B phase, O atoms are located in voids with tetrahedral arrangement within the hcp structure.¹¹¹ Notably, Tb–Tb distances are 3.278, 3.536, 3.657, and 4.114 Å in B-type Tb_2O_3 at room pressure,¹⁰⁸ giving an average Tb–Tb distance of 3.646 Å that is only slightly larger (3.4%) than the Tb–Tb distance in hcp Tb (3.525 Å).¹¹²

Full pattern matching of B-type Tb_2O_3 allowed us to extract its lattice parameters on the upstroke between 7 and 11 GPa and also on the downstroke from 10 GPa down to room pressure. As expected, a monotonous decrease of the unit-cell

volume of B-type Tb_2O_3 up to 11 GPa is observed (Figure 4). Fit of pressure vs. experimental unit-cell volume to a second-order BM-EoS yields $V_0 = 426.1(5) \text{ \AA}^3$ and $B_0 = 133(3) \text{ GPa}$, respectively. In this case, we rely on the second-order EoS because third-order terms do not better explain the normalized stress vs. Eulerian strain dependence for this phase (not shown). The results thus obtained are in very good agreement with the results of our theoretical GGA-PBE calculations: a fit to a second-order BM-EoS yields $V_0 = 428.8(1) \text{ \AA}^3$ and $B_0 = 135.3(6)$. It can be observed that the room-pressure unit-cell volume, lattice parameters, and monoclinic β angle obtained in this work for B-type Tb_2O_3 agree nicely with those previously obtained (see Tables 1 and 2).^{10,107,108} Additionally, the B_0 value is similar to that found in Eu_2O_3 ¹¹³ but smaller than that of Y_2O_3 .¹¹⁴

The experimental lattice parameters of B-type Tb_2O_3 up to 12 GPa (see Figure 5a) display a monotonous and smooth

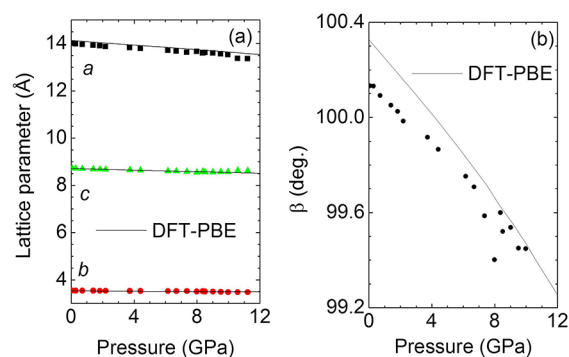


Figure 5. Experimental (symbols) and theoretical (lines) pressure dependence of the lattice parameters and β monoclinic angle of B-type Tb_2O_3 . The calculated errors for the refined lattice parameters and monoclinic β angle are smaller, in all cases, than the symbol sizes.

decrease as pressure increases in good agreement with our theoretical GGA-PBE calculations. Similarly, the experimental and theoretical pressure dependences of its axial ratios c/b , a/b , and a/c (see Figure S5) are also found to display a monotonous behavior that is well reproduced by our calculations. On the other hand, a small reduction of the monoclinic β angle (see Figure 5b), always perpendicular to the b -axis, is found at HP. This result implies that the direction of the a -axis in B-type Tb_2O_3 displays a slight change with pressure (assuming that the directions of both the b - and c -axes remain constant). All these observations, as well as the good agreement between the GGA-PBE calculations and experimental results, support the present theoretical description of the compression of B-type Tb_2O_3 . The analysis of the theoretical and experimental compressibility tensors of this phase (see Tables S9 and S10 in the SI) shows that the a -axis of the monoclinic cell is more compressible than the b - and c -axes in the whole pressure range of stability of this phase. On the other hand, the theoretical pressure dependence of the Tb–O distances in B-type Tb_2O_3 (see Figure S6) shows that, with the exception of one of the Tb_1 –O and Tb_3 –O distances, there is a monotonous decrease of the Tb–O distances at HP similar to that found for the C-type phase. This plot reflects that there is also no net increase of the Tb coordination at HP for any of the three independent Tb atoms in this phase. It also reflects the complex rearrangement of the different atoms of the monoclinic cell upon compression, which ends up with the

B \rightarrow A PT. Indeed, the B \rightarrow A PT is of weak first-order character since it shows a very small volume reduction (<2% according to GGA-PBE calculations).

The trigonal A-type Tb₂O₃, shown in Figure 1c, is characterized by having one Tb atom at a 2d site, one O atom (O1) at a 2d site, and one O atom (O2) at a 1a Wyckoff site. Therefore, this structure has only two free atomic coordinates corresponding to the *z* atomic positions of the two atoms at 2d sites. In A-type Tb₂O₃, Tb is 7-fold coordinated; O1 is 4-fold coordinated, and O2 has 6-fold coordination. This means that on average the coordination of O atoms is 5, very similar to that of the B-type structure, while the coordination of Tb is slightly larger than in the B-type structure. This result is in agreement with the A-type phase being related to the B-type structure (which is a distortion of the former). Therefore, it can be concluded that the A-type phase is also characterized by a cation array similar to the hcp structure of metals, like the B-type phase.¹¹¹ Note that the B-type structure derives from the A-type phase by a slight lattice deformation implying a splitting of 1a (D_{3d}) and 2d (C_{3v}) atomic positions into less symmetrical 2b (C_{2h}) and 4i (C_s) sites, as commented by Goutheron et al.¹¹⁵

Whole pattern matching of A-type Tb₂O₃ XRD scans allowed us to get the lattice parameters of this phase on upstroke from 12 to 20 GPa. As expected, a monotonous decrease of the unit-cell volume of A-type Tb₂O₃ is observed at HP (Figure 4). Fit of pressure vs experimental unit-cell volume to a second-order BM-EoS yields $V_0 = 71.0(6) \text{ \AA}^3$ and $B_0 = 112(5) \text{ GPa}$. As already commented, there is no previous experimental published data in the literature for this phase of Tb₂O₃. It must be stressed that, again, our theoretical GGA-PBE data follow rather closely the experimental results. The fit of theoretical data to a second-order BM-EoS yields $V_0 = 70.3(1) \text{ \AA}^3$ and $B_0 = 134(1) \text{ GPa}$. As observed, our theoretical B_0 is slightly larger than the experimental one. The difference between them will be discussed later. In this context, we can mention that the experimental B_0 of Tb₂O₃ is similar to that of Ce₂O₃¹¹⁶ and smaller than that of Nd₂O₃.¹¹⁷

The pressure dependence of the lattice parameters of the trigonal A-type Tb₂O₃ (see Figure 6) shows a monotonous

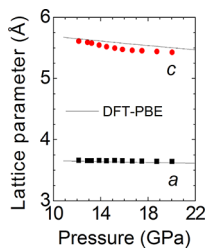


Figure 6. Experimental (symbols) and theoretical (lines) pressure dependence of the lattice parameters of A-type Tb₂O₃. The calculated errors for the experimental lattice parameters are smaller than the symbol sizes.

decrease of both *a* and *c* lattice parameters at HP and a relatively good agreement between the experimental and theoretical results. It must be noted that the experimental (theoretical) value of the *c/a* ratio for A-type Tb₂O₃ at 12.2 GPa is 1.534 (1.548) according to data in Table 2. In turn, the theoretical value expected at 0 GPa for A-type Tb₂O₃ is 1.577, while that of A-type Y₂O₃ is of 1.617.⁷⁹ Interestingly, it has been suggested that the *c/a* ratio of A-type RE SOs from La₂O₃

to Sm₂O₃ tends to the ideal value of 1.633 that corresponds to the hexagonal close packing of cations.¹¹⁵ However, such a value is not observed in any theoretical estimation of the RE SOs, including A-type Y₂O₃ and A-type Sc₂O₃. In fact, all theoretical *c/a* values of A-type RE SOs (including Y₂O₃) remain below 1.62, except for Sc₂O₃ that is around 1.67.⁷⁹ Therefore, it seems that the relationship between the distortion of the hexagonal close packing of cations and the ionic radius seems not to be a valid idea for A-type RE SOs.

The pressure dependence of the *c/a* ratio in A-type Tb₂O₃ (see Figure S7) shows a decrease of both experimental and calculated values at HP. This means that the ratio progressively deviates from the ideal value of the hexagonal close packing of cations as pressure increases. The experimental curve, however, exhibits a kink around 15 GPa that is probably a consequence of the broad XRD reflections that are detected for this phase, giving rise to large experimental errors in the determination of the lattice parameters. Figure S8a,b shows the pressure dependence of the theoretical free atomic coordinates and Tb–O distances in A-type Tb₂O₃. As observed, the GGA-PBE calculations predict almost no change in the two free atomic parameters (z_{Tb} , z_{O}) with increasing pressure as well as a monotonous decrease of Tb–O distances, with no sudden changes that could give rise to the kink observed in the experimental *c/a* ratio. As it was already commented for the case of the C- and B-type phases, it can be concluded that the decrease of Tb–O distances at HP in A-type Tb₂O₃ is fully determined by the lattice parameter reduction due to the negligible change in the free atomic parameters at HP and that no net increase of Tb coordination seems to occur in the A-type phase with increasing pressure up to 24 GPa. We want to note that the change of the free atomic parameters with increasing pressure in B-type Tb₂O₃ (not shown) is also rather small, although not negligible. These results are consistent with the negligible change of theoretical free atomic parameters of both B-type and A-type phases on the changing ionic radius.⁷⁹ In fact, the experimental free atomic parameters of B-type Sc₂O₃ at 38.5 GPa⁴⁸ are similar to the theoretical ones reported for Sc₂O₃ at 0 GPa by Wu et al.⁷⁹ and at 15.7 GPa by Zhang et al.¹¹⁸ In this context, we must note that a value of 0.5 must be added to experimental values of the free coordinate *x* of Sc atoms and of O(4) and O(5) atoms in ref 48 (due to a lattice origin shift) for a proper comparison with the theoretical values plotted in Figure S8a.

4.2. Compression Behavior of RE and Related Sesquioxides. Next, we would like to compare the bulk moduli of A-, B-, and C-type Tb₂O₃ with those of other RE SOs and isostructural SOs. Only a few works have attempted to understand the overall compression behavior of this family of materials.^{84,86} For this purpose, we have summarized in Table S1 the experimentally reported values of the bulk moduli of some of these compounds in the C-type/bixbyite structure. As already discussed,⁸⁴ experimental data show considerable dispersion, making it almost impossible to draw any conclusion about the behavior of the bulk moduli of C-type SOs. To address this issue, here we have performed theoretical DFT-PBE calculations for several known C-type SOs, including Sc₂O₃, Y₂O₃, In₂O₃, Sm₂O₃, Gd₂O₃, Tb₂O₃, Lu₂O₃, and Tl₂O₃ corresponding to atomic numbers 21, 39, 49, 62, 64, 65, 71, and 81. Moreover, we have also performed the same calculations for Al₂O₃, Fe₂O₃, Ga₂O₃, V₂O₃, Mn₂O₃, Cm₂O₃, Pu₂O₃, Eu₂O₃, Nd₂O₃, and La₂O₃ in order to extend the range of cation ionic radii in possible C-type/bixbyite SOs. Figure

S9a shows a rather good agreement of our theoretical and reported experimental unit-cell volume pfu in almost all C-type SOs, with an upward sawtooth-like tendency with an increasing atomic number. Contrarily, our theoretical bulk moduli show a systematic slight underestimation of the corresponding experimental data (Figure S9b), but both the experimental and theoretical values show a clear overall tendency to decrease with increasing Z . This result suggests that the reduction of the bulk modulus (i.e., increase of the compressibility) with Z is in fact related to the corresponding unit-cell volume increase. Opposite to the overall tendency, the region corresponding to the RE SOs shows a decrease (increase) of the zero-pressure volume (bulk modulus) with increasing Z , in good agreement with previous calculations.^{80,86}

It can be observed that our theoretical GGA-PBE calculations slightly overestimate the experimental volumes, with the largest differences being found in In_2O_3 (~5%) and Tl_2O_3 (~7%). The lanthanide contraction effect is well reproduced by our calculations and agrees well with previous works.^{73,75,80,84,86} Noteworthy, the largest deviations in the theoretical vs experimental bulk modulus also correspond to In_2O_3 (~22%) and Tl_2O_3 (~28%). The large deviations for these two compounds, observed in light of the comparison between their theoretical and their well-known experimental unit-cell volumes in Figure S9a, suggest that the theoretical values are clearly underestimated, whereas the experimental bulk moduli are likely quite overestimated. On the other hand, the comparison of our theoretical estimations and experimentally reported B_0 values for RE SOs suggests that the experimental B_0 values reported for Dy_2O_3 , Gd_2O_3 , and Yb_2O_3 seem to be quite overestimated, whereas that of Lu_2O_3 seems to be rather underestimated.

In Figure 7a, we have plotted the experimental and theoretical unit-cell volume pfu as a function of the third power of the cation ionic radius, r^3 , in C-type SOs. It can be observed that there is a clear linear trend between both parameters (see red circles and red line), as already established by Shannon and Prewitt in 1970.¹²⁰ This linear dependence is a direct consequence of the negligible change of the free atomic parameters of the C-type structure when changing the cation ionic radius, as already discussed. Moreover, the linear dependence between unit-cell volume and r^3 implies that there cannot be a linear relationship between the unit-cell volume of C-type SOs and the cation ionic radius, as initially suggested by Hoekstra in 1966.¹⁰⁷ In fact, our theoretical calculations for the C-type phase show a relationship between the unit-cell volume and cation ionic radii (not shown) similar to that reported for B- and A-type phases in ref 79. In this context, we must stress that our calculations are more comparable to GGA+U calculations for RE SOs than to WC-GGA ones.⁸⁴ Moreover, our calculations allow us to extend the observed trend even farther than previously reported (from Al_2O_3 to La_2O_3). As observed, the largest deviation of theoretical values from experimental values are those of cubic In_2O_3 , Tl_2O_3 , and Fe_2O_3 . This suggests that GGA-PBE is not the best method to describe the unit-cell volume for these three compounds. Furthermore, our graph suggests that the experimental unit-cell volume reported for C-type Fe_2O_3 ¹²¹ either does not follow the linear trend of other C-type SOs or is considerably overestimated. In fact, our calculations estimate the unit-cell volume per formula unit of C-type Fe_2O_3 to be around 47.32 \AA^3 .

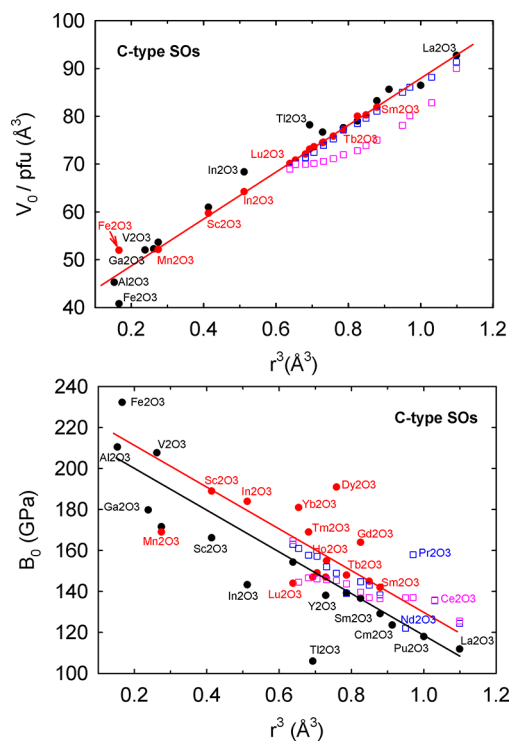


Figure 7. Experimental (red symbols) and theoretical (black symbols) unit-cell volume per formula unit (a) and bulk modulus (b) of C-type sesquioxides as a function of the cube cation ionic radius. Theoretical data of ref 84 with WC-GGA (pink open squares) and GGA+U (blue open squares) are also shown for comparison. Red lines show the linear trend in experimental values, while the black line suggests the linear trend in theoretical bulk modulus according to our calculations. Cation ionic radii have been taken from ref 119 for valence 3+ with 6-fold coordination.

In Figure 7b, we show the experimental and theoretical B_0 values as a function of r^3 in C-type SOs. Again, a linear trend can be plotted between both parameters (see red circles and red line). Note that our calculated values display rather good agreement with previous ones.⁸⁴ The negative slope of the B_0 values with the third power of the cation ionic radius clearly shows the inverse relationship between the bulk modulus and the unit-cell volume. Thus, with the exception of the lanthanides due to the contraction effect, the increase of cation Z leads in general to larger cation ionic radius, larger unit-cell volumes, and smaller bulk moduli. Our graph shows that our calculated B_0 values are somewhat underestimated as compared to experimental ones. Similar to the case of the unit-cell volume, the largest underestimation corresponds to In_2O_3 and Tl_2O_3 . Additionally, we think that the theoretical B_0 value of C-type Fe_2O_3 is somewhat overestimated and a value close to 220 GPa should be expected. Unfortunately, there is no reported bulk modulus, to our knowledge, for this metastable phase of Fe_2O_3 .

Interestingly, similar conclusions to those here obtained for the C-type/bixbyite phase of SOs can be reached for the B- and A-type phases of RE SOs. Figures S10a and S11a show the increase of the unit-cell volume pfu in B- and A-type RE SOs with increasing Z , except along the lanthanide series due to the lanthanide contraction effect. Our calculations are in good agreement with other theoretical calculations.^{80,84,86} Contrarily, B_0 shows the opposite trend and decreases with increasing Z , except along the lanthanide series. As observed, our

experimental and theoretical values for the B_0 values of B- and A-type Tb_2O_3 are within the error margin, and it seems that the experimental B_0 value of the A-type phase is somewhat underestimated due to the difficulties in obtaining the lattice parameters of this phase, as already commented.

Figures 8a and 9a show the theoretical (GGA-PBE) V_0 value per pfu as a function of r^3 for some RE SOs, including Sc_2O_3 and

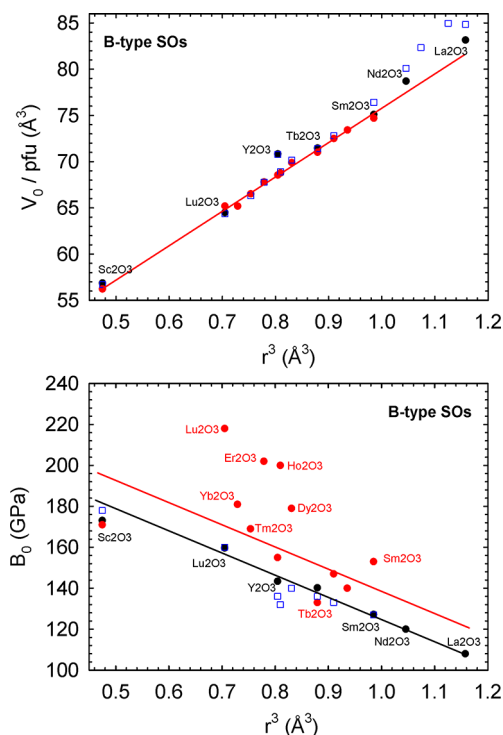


Figure 8. Experimental (red symbols) and theoretical (black symbols) unit-cell volume per formula unit (a) and bulk modulus (b) of B-type sesquioxides as a function of the third power of the cation ionic radius (r^3). Theoretical data of ref 79 (blue open squares) are also shown for comparison. Red lines show the linear trend in experimental values, while the black line indicates the linear trend in theoretical bulk modulus according to our calculations. Cation ionic radii have been taken from ref 119 for valence 3+ with 6.5-fold coordination.

Y_2O_3 , with B- and A-type structures, respectively. Data for other SOs (without f orbitals) are not included in the plot because these materials do not exhibit these two phases. It can be observed that there is a linear relationship between both parameters in both phases. Again, the linear behavior between V_0 values of the B- and A-type structures and the third power of the cation ionic radius is a direct consequence of the negligible change of the free atomic parameters in both structures with the cation ionic size, as already discussed. We have to stress that both experiments and calculations show that there is no linear relationship between V_0 of B-type and A-type SOs and the cation ionic radius, as initially suggested by Hoekstra.¹⁰⁷ This conclusion is especially clear when data from Sc_2O_3 to La_2O_3 are included to extend the range of ionic radii. In this context, our theoretical calculations compare rather well with calculations for B- and A-type RE SOs.⁷⁹ As observed, the largest deviation of theoretical values from experimental values are those for Y_2O_3 .

In turn, Figures 8b and 9b show the theoretical (GGA-PBE) B_0 values as a function of r^3 for some RE SOs, including Sc_2O_3 and Y_2O_3 , with B- and A-type structures, respectively. As can

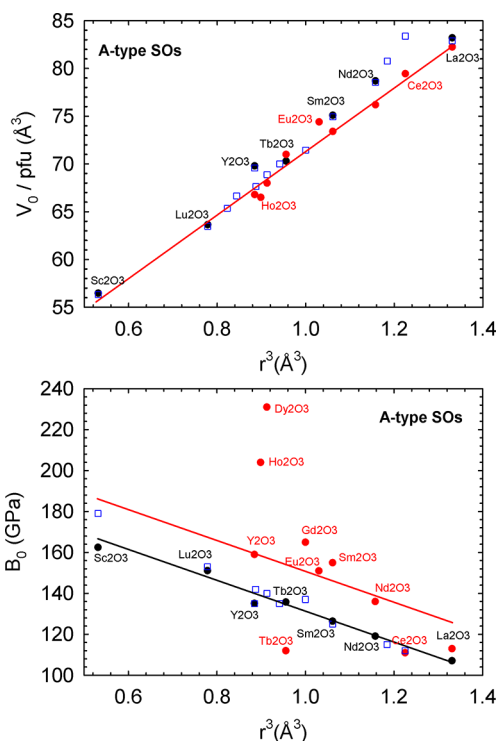


Figure 9. Experimental (red symbols) and theoretical (black symbols) unit-cell volume per formula unit (a) and bulk modulus (b) of A-type sesquioxides as a function of the third power of the cation ionic radius (r^3). Theoretical data of ref 79 (blue open squares) are also shown for comparison. Red lines show the linear trend in experimental values, while the black line indicates the linear trend in theoretical bulk modulus according to our calculations. Cation ionic radii have been taken from ref 119 for valence 3+ with 7-fold coordination.

be seen in both figures, there is a linear relationship between B_0 and r^3 for both B- and A-type structures that suggests an almost inverse relationship between the B_0 and V_0 for the A- and B-type phases of the RE SOs, including Sc_2O_3 and Y_2O_3 . Moreover, the comparison of theoretical and experimental data may suggest that the B_0 values of B-type Lu_2O_3 , Er_2O_3 , Dy_2O_3 , and Ho_2O_3 seem to be quite overestimated and the same holds for A-type Dy_2O_3 and Ho_2O_3 , while those of A-type Tb_2O_3 and Ce_2O_3 are likely underestimated. We have to note that our results on the linear behavior of B_0 values of B- and A-type SOs with respect to the cube cation ionic radius are in agreement with previous calculations.⁷⁹

Finally, we want to comment about the B_0 values in C-, B-, and A-type SOs. In general, HP phases show larger densities than low pressure phases and correspondingly higher bulk moduli. This means that the A-type phase should have a larger bulk modulus than the B-type phase and the latter one, a larger one than the C-type phase, assuming a C–B–A sequence of PTs as in Tb_2O_3 . However, this trend has not been observed in a number of RE SOs, including Tb_2O_3 (see Table 1). It was previously noted that theoretical values for the bulk modulus of the B-type (A-type) SOs are in general slightly higher (lower) than those of C-type SOs,⁷⁹ but this was not supported by ref 84, which reports a bulk modulus of A-type SOs 10–15% higher than that of C-type SOs. On the other hand, theoretical B_0 values larger for the B-type phase than for the A-type phase were suggested by another theoretical work.⁷⁶

In this context, we have tried to revise these apparently contradictory results using our theoretical calculations and the

linear trends shown by the B_0 values of A-, B-, and C-type phases with the third power of the cation ionic radius and to answer old questions related to the B_0 values in C-, B-, and A-type SOs: Which phase exhibits the largest B_0 value? Is there an order of increasing B_0 values for the different phases of RE SOs?

To this aim, we have joined our theoretical results from Figures 7b, 8b, and 9b into a single one (see Figure S12). As observed, the slopes of the linear trends for the C- and B-type structures follow parallel paths, but this is not the case for the A-type structure. On the other hand, the use of different Shannon ionic radii for each structure, due to the different average coordination of cations in each structure, poses a problem. It leads to three different positions for each Ln atom, one corresponding to each structure. To simplify this picture, we have plotted in Figure 10 the theoretical B_0 values for each

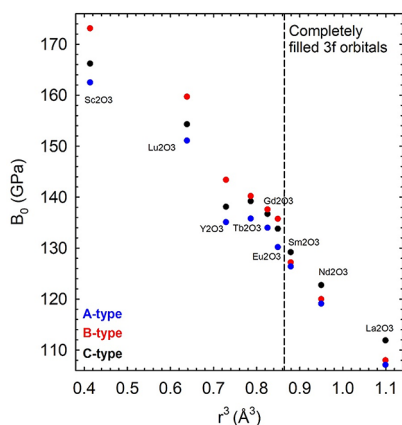


Figure 10. Theoretical (symbols) bulk modulus of C-type (black), B-type (red), and A-type (blue) RE-SOs as a function of the third power of the cation ionic radius (r^3). Note that cation ionic radii have been taken from ref 119 for valence 3+ with 6-fold coordination for all C-, B-, and A-type crystalline structures so that all bulk moduli for a single cation lie in a vertical fashion.

Ln_2O_3 compound in the three structures vs the third power of the cation ionic radius but assigning one single cation ionic radius for each Ln atom (for instance, the one for 6-fold coordination). In that way, all three B_0 values lie in vertical fashion. Surprisingly, this ordering shows that the order of B_0 values for A-, B-, and C-type phases is completely different for small- and medium-sized cations (Sc–Eu) than for medium and big cations (Sm–La). More specifically, we can see that small cations show a larger bulk modulus for the B-type phase, followed by the C- and A-type phases in agreement with ref 79. On the contrary, large cations show a larger bulk modulus for the C-type phase, followed by the B- and A-type phases. Besides, we have found that B_0 values for the B-type phase are always larger than those for the A-type phase, in agreement with ref 76. Curiously, the B_0 values for the B- and A-type phases are very close to each other for large cations and are very different for small cations. Therefore, we can see that the change of ordering of the B_0 values lays between Eu_2O_3 and Sm_2O_3 ; i.e., large Ln atoms (up to 3 f orbitals filled) show a completely different behavior than smaller Ln atoms (with more than 3 f orbitals filled). Therefore, we can ascribe the different mechanical properties of the three phases of RE SOs to the presence or not of the first 3 filled f orbitals in Ln atoms. In addition, this different ordering of B_0 values could be related

to the larger stability of B- and A-type structures in large cations and of the C-type structure in the smallest cations. Note that the C-type structure is not the stable phase for large cations, where the B_0 values of the C-type structure are considerably higher than those for B- and A-type structures.

In summary, we have proved that our theoretical calculations for different C-, B-, and A-type SOs reproduce the well-known lanthanide unit-cell volume contraction with the increase of the atomic number as well as the inverse linear relationship between the bulk modulus for the three phases and the unit-cell volume, or equivalently, the third power of the cation ionic size; however, differences in the ordering of the bulk modulus values have been found between large and small Ln cations. Consequently, we can conclude that the compressibility of the C-, B-, and A-type phases of RE SOs is mainly determined by the unit-cell volume and correspondingly by the cation ionic radii as well as by the filling or not of the first three f orbitals. In this way, we have shown a general overview of the behavior of RE SOs under compression that complements the one recently reported for phase transition pressures.¹⁵ Moreover, we have extended the discussion regarding the linear dependence of the unit-cell volume and bulk moduli of RE SOs (including Sc_2O_3 and Y_2O_3) vs the cube cation ionic size to other C-type/bixbyite-type SOs. On top of that, we have found that our experimental bulk moduli for the different phases of Tb_2O_3 are within the error margin of measurements, likely being the experimental bulk modulus of A-type Tb_2O_3 being slightly underestimated. Besides, we have pointed out that several experimental bulk moduli of SOs must be revised since they seem to be quite different from the expected results.

4.3. Vibrational Properties of Tb_2O_3 under Pressure: Comparison to Related Sesquioxides.

RS spectroscopy is a powerful nondestructive analytical tool that provides useful information, among others, about the crystal quality, structural properties, and lattice dynamics of solid state materials. Many different studies have been devoted to investigate the vibrational properties of C-type RE SOs (see ref. 122 and references therein) as well as of B-type and A-type RE SOs.^{115,123,124} It should be noted that powder XRD is not able to discern between the trigonal A-type phase and the hexagonal H-type phase since both yield very similar powder XRD patterns.¹²⁵ However, these two phases have sizably different vibrational properties due to the fact that the H-type phase has twice the number of formula units than the A-type phase. As will become evident below, the present HP-RS measurements in Tb_2O_3 confirm both the cubic-to-monoclinic (C → B) and the monoclinic-to-trigonal (B → A) PTs in this compound.

Group theory predicts that the cubic C-type structure ($Ia\bar{3}$) should have 120 zone-center vibrational modes: $\Gamma_{120} = 4A_g(\text{R}) + 4E_g(\text{R}) + 14F_g(\text{R}) + 5A_u + 5E_u + 17F_u(\text{IR})$, where E and F modes are double and triple degenerate, respectively (F modes are also denoted as T in some works). The 22 gerade (g) modes are Raman-active (R) modes; the 16 F_u modes are infrared (IR)-active modes, and the A_u and E_u are silent modes. One F_u mode corresponds to the acoustic vibrations. In regard to the monoclinic B-type structure ($C2/m$), group theory predicts 42 zone-center vibrational modes: $\Gamma_{42} = 14A_g(\text{R}) + 7B_g(\text{R}) + 7A_u(\text{IR}) + 14B_u(\text{IR}) + A_u + 2B_u$. The 21 gerade (g) modes are Raman-active (R) modes, while 21 ungerade (u) modes are infrared (IR)-active modes, and one A_u and two B_u modes correspond to the acoustic vibrations. Finally, the trigonal A-type structure ($P\bar{3}m1$) should have the following 15

zone-center vibrational modes: $\Gamma_{15} = 2A_{1g}(\text{R}) + 2E_g(\text{R}) + 2A_{2u}(\text{IR}) + 2E_{2u}(\text{IR}) + A_{2u} + E_u$. The 4 g modes are Raman-active; the 4 u modes are IR-active, and one A_{2u} mode and one E_u mode correspond to the acoustic vibrations. Finally, it should be mentioned that group theory predicts that the hexagonal H-type structure ($P6_3/mmc$) should have 30 zone-center vibrational modes because it has two formula units per unit cell: $\Gamma_{30} = 2A_{1g}(\text{R}) + 2E_{1g}(\text{R}) + 2E_{2g}(\text{R}) + 2A_{2u}(\text{IR}) + 3E_{1u}(\text{IR}) + 3B_{2u} + 3E_{2u} + A_{2u} + E_{1u}$. The 6 g modes are Raman-active; 5 u modes are infrared (IR)-active, and 6 u modes are silent. One A_{2u} mode and one E_{1u} mode correspond to the acoustic vibrations. Therefore, as will be evident below, the number of observed Raman-active modes may allow one to distinguish between the trigonal A and hexagonal H structures.

We have recently characterized the Raman-active modes of C-type Tb_2O_3 at room pressure.⁸⁹ In the present work, we have performed unpolarized RS measurements and observed up to 16 out of 22 Raman-active modes of the cubic phase as a function of pressure (see Figure 11). It can be observed that

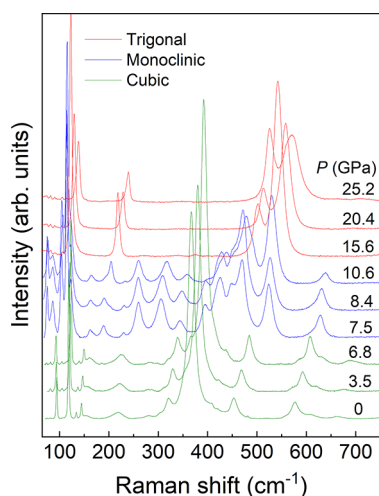


Figure 11. Room-temperature Raman spectra of Tb_2O_3 at selected pressures up to 25 GPa.

the cubic phase is stable from 0 to 6.8 GPa and has completely disappeared at 7.5 GPa. Above 6.8 GPa, new Raman peaks emerge in the spectra that have been attributed to the monoclinic B-type phase. In particular, a very weak feature at 185 cm^{-1} is observed at that pressure, despite the new phase being only clear above 7.5 GPa. RS spectra indicate that the monoclinic phase is stable up to 10.6 GPa, in agreement with our XRD results. At 11.5 GPa, other Raman peaks showed up, as evidenced by the appearance of features at 490 and 530 cm^{-1} that have been attributed to the trigonal A-type phase. Finally, the A phase, that shows four Raman bands, was found to back-transit, on the downstroke, to the B-type phase below 10.4 GPa. The B-type phase was fully recovered at 8.4 GPa and, similarly to our XRD results, it was found to be metastable down to 0 GPa. Therefore, Raman data confirm not only the two PTs observed by HP-XRD but also the trigonal A-type nature of the HP phase above 12 GPa, as it only displays 4 Raman-active modes.

In order to help in the identification of this metastable phase, the RS spectrum of the B-type phase at room pressure is plotted in Figure 12, together with the theoretical zero-pressure wavenumbers according to GGA-PBE and GGA-PBESol DFT calculations. As can be seen in the figure, the PBE

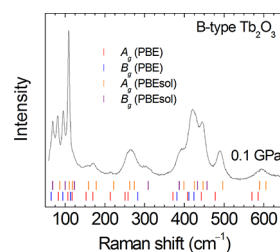


Figure 12. Room-temperature Raman spectrum of the recovered monoclinic B-type phase of Tb_2O_3 at room pressure. Pressure is somewhat larger ($\sim 0.1\text{ GPa}$) than ambient pressure because the DAC was not open to perform this measurement. The vertical ticks indicate calculated frequencies for A_g and B_g modes with DFT-PBE (lower ticks) or DFT-PBESol (upper ticks).

functional provides better results in the case of the low-wavenumber modes ($<250\text{ cm}^{-1}$). In contrast, PBESol seems to be in better agreement for the high-wavenumber modes ($>250\text{ cm}^{-1}$). While PBESol clearly underestimates the unit-cell volume of both the C-, B-, and A-type phases of Tb_2O_3 , the reduced interatomic distances predicted in this case seem to yield increased spring constants and therefore improved results in the case of the high-wavenumber modes (with mainly O vibrations as shown in ref 89). From now on, we rely on the GGA-PBE vibrational results as this functional better reproduces both the compression behavior of the unit-cell volume and the low-wavenumber modes (with mainly Tb vibrations).

Figure 13 shows the experimental (on upstroke) and theoretical wavenumbers of the Raman-active modes in

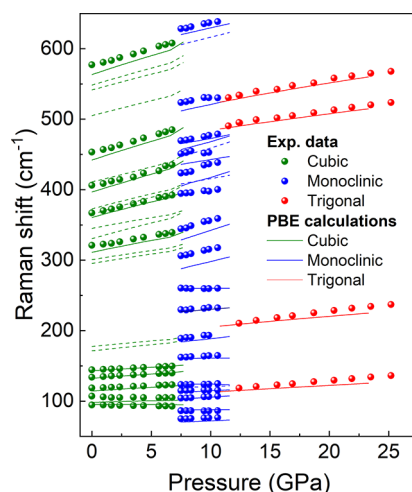


Figure 13. Experimental (symbols) and theoretical DFT-PBE (lines) pressure dependence of the Raman-active mode wavenumbers in cubic (green), monoclinic (blue), and trigonal (red) Tb_2O_3 with increasing pressure. Solid (dashed) lines correspond to observed (unobserved) Raman-active modes.

Tb_2O_3 as a function of pressure up to 25 GPa. As can be seen in the plot, the pressure dependence of the theoretical wavenumbers of the Raman-active modes is in good agreement with our experimental results and almost all wavenumbers shift to higher frequencies due to the shortening of bond lengths as a consequence of the volume decrease at HP. Additionally, we have plotted in Figure 14 the pressure dependence of the experimental (on the downstroke) and theoretical Raman-

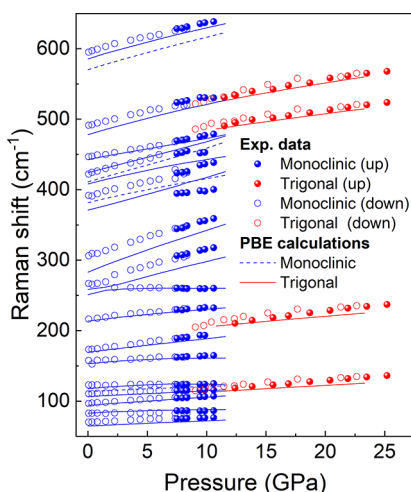


Figure 14. Experimental (symbols) and theoretical DFT-PBE (lines) pressure dependence of the Raman-active mode wavenumbers in monoclinic and trigonal Tb_2O_3 . Experimental data on increasing pressure (solid symbols) and decreasing pressure (empty symbols) are plotted for comparison. Solid (dashed) lines correspond to observed (unobserved) Raman-active modes.

active mode wavenumbers of B- and A-type Tb_2O_3 from 25 GPa down to room pressure but also including the experimental upstroke values of these two phases shown in Figure 13. These data on the downstroke have allowed us to get the full pressure dependence of the Raman-active modes of the B-type phase. The experimental and theoretical wavenumbers and pressure coefficients of the Raman-active optical phonons of Tb_2O_3 in the C-, B-, and A-type phases can be found in Tables 3, 4, and 5, respectively.

As observed in Figures 13 and 14 and in the corresponding tables, a good agreement is found between our experimental and theoretical lattice-dynamical results. Moreover, the comparison between the calculated and experimental wavenumbers and pressure coefficients allows us to assign the symmetries of the different Raman peaks from the two HP phases with a high degree of certainty. This is particularly useful, as polarized measurements are not feasible for these phases. The symmetries of the different modes are displayed in the first column of these three tables.

The pressure dependence of the Raman-active mode wavenumbers of C-type Tb_2O_3 shown in Figure 13 is similar to that reported for C-type Lu_2O_3 ,^{16,17} Yb_2O_3 ,¹⁹ Tm_2O_3 ,²¹ Sc_2O_3 ,⁵⁰ Y_2O_3 ,⁵¹ and In_2O_3 .⁶⁹ Similarly, the pressure behavior of the Raman-active mode wavenumbers of B-type Tb_2O_3 shown in Figures 13 and 14 is similar to that reported in the literature for B-type Lu_2O_3 ,^{16,17} Yb_2O_3 ,¹⁹ Tm_2O_3 ,²¹ Y_2O_3 ,⁵¹ and Sm_2O_3 .^{47,126} Finally, the pressure dependence of Raman-active modes of A-type Tb_2O_3 shown in Figures 13 and 14 is similar to that reported for A-type Sm_2O_3 ^{47,126} and Nd_2O_3 .¹²⁷ The wavenumbers and pressure coefficients for the Raman-active modes in the different phases of Tb_2O_3 can be compared with those of other RE SOs. In Tables S3 and S4, we have compared the experimental and theoretical zero-pressure Raman mode wavenumbers and pressure coefficients of several C-type SOs, respectively. On the other hand, in Tables S5 and S6, we have compared the experimental Raman mode wavenumbers and pressure coefficients of several B-type and A-type SOs, respectively.

Table 3. Experimental (Upstroke) and DFT-PBE Theoretical Zero-Pressure Wavenumbers (in cm^{-1}) and Linear Pressure Coefficients (in $\text{cm}^{-1}\text{GPa}^{-1}$) for the Raman-Active Modes of C-type Tb_2O_3

symmetry	theoretical		experimental	
	ω_0	$d\omega/dP$	ω_0	$d\omega/dP$
F_g^1	95.05	-0.06	94.5	-0.25
F_g^2	98.36	0.36	106.2	-0.24
A_g^1	114.29	0.96	118.6	0.68
F_g^3	132.35	1.13	134.2	0.87
E_g^1	143.13	0.93	144.4	0.78
F_g^4	171.36	1.70		
F_g^5	177.48	1.52		
F_g^6	295.32	2.61		
F_g^7	300.68	2.57		
E_g^2	311.07	3.32	320	2.86
F_g^8	330.57	4.33		
A_g^2	345.04	2.92		
F_g^9	360.67	4.26	366.7	3.86
E_g^3	365.13	4.74		
F_g^{10}	372.74	4.08		
A_g^3	396.77	5.08	404.7	4.33
F_g^{11}	411.15	4.44		
F_g^{12}	442.06	5.32	452.4	4.76
F_g^{13}	505.15	4.28		
A_g^4	541.45	4.51		
E_g^4	548.42	4.83		
F_g^{14}	563.49	5.30	576.4	4.76

Table 4. Experimental and DFT-PBE Theoretical Zero-Pressure Wavenumbers (in cm^{-1}) and Linear Pressure Coefficients (in $\text{cm}^{-1}\text{GPa}^{-1}$) for the Raman-Active Modes of B-type Tb_2O_3 ^a

symmetry	theoretical		experimental	
	ω_0	$d\omega/dP$	ω_0	$d\omega/dP$
B_g^1	64.58	0.73	70.3	0.7
A_g^1	82.90	0.37	82.9	0.01
B_g^2	94.05	1.15	96.8	1.16
A_g^2	106.55	0.82	110.8	0.64
A_g^3	113.64	0.68		
B_g^3	117.37	0.39	122.9	0.13
A_g^4	152.90	0.61	156.3	0.88
A_g^5	169.61	1.89	172.8	2.14
A_g^6	213.53	1.57	216.5	1.8
A_g^7	250.99	0.47	261.8	-0.23
A_g^8	258.47	4.13	265.2	5.09
B_g^4	282.94	5.77	306.6	5.12
B_g^5	371.05	4.73	368.6	1.73
A_g^9	381.52	3.29		
A_g^{10}	408.19	3.27	391.7	3.77
B_g^6	411.25	4.86		
A_g^{11}	424.18	4.48	426.2	2.43
B_g^7	442.58	3.03	446.0	2.95
A_g^{12}	477.94	4.13	492.0	3.59
A_g^{13}	570.26	4.49		
A_g^{14}	585.39	4.24	596.7	3.92

^aFor the fits of experimental data, the upstroke and downstroke results have been used. The pressure dependence of all wavenumbers has been fitted to a linear polynomial in the low pressure range (0–2 GPa).

Table 5. Experimental (Upstroke) and DFT-PBE Theoretical Wavenumbers (in cm^{-1}) at 11 GPa and Linear Pressure Coefficients (in $\text{cm}^{-1}\text{GPa}^{-1}$) for the Raman-Active Modes of A-type Tb_2O_3

symmetry	theoretical		experimental	
	$\omega(P = 11 \text{ GPa})$	$d\omega/dP$	$\omega(P = 11 \text{ GPa})$	$d\omega/dP$
E_g^1	113.7	0.95	116.0	1.40
A_{1g}^1	206.6	1.47	207.7	2.07
A_{1g}^2	486.6	2.28	490.3	2.32
E_g^2	524.7	2.87	529.2	2.79

In regard to the lattice dynamics of C-type SOs, several works have recently addressed the comparison of Raman-mode wavenumbers in C-type SOs.^{89,122} In this work, we will concentrate on the comparison of the pressure coefficients provided in Tables S3 and S4. In particular, the large difference in mass of the Ln cations and O anions has allowed us to distinguish two regions: the low-wavenumber region (below 250 cm^{-1}) dominated by pure Ln vibrations and the high-wavenumber region (above 250 cm^{-1}) dominated by pure oxygen vibrations. One additional subdivision can be added to the high-wavenumber region since Raman-active modes in C-type RE SOs show phonon gaps between the different regions. In this way, we can establish: (i) the low-wavenumber region below 250 cm^{-1} ; (ii) the medium-wavenumber region between 250 and 550 cm^{-1} ; (iii) the high-wavenumber region above 550 cm^{-1} . The modes in the medium-wavenumber region are generally bending Ln–O modes, while those in the high-wavenumber region are generally stretching Ln–O modes. In general, the theoretical pressure coefficients of the vibrational modes increase with increasing wavenumber in C-type SOs. This means that the smallest pressure coefficients must be found in the low-wavenumber region, while the largest pressure coefficients are found in the medium- and high-wavenumber regions. In particular, the three highest-wavenumber modes (A_g^4 , E_g^4 , and F_g^{14}) are always among the Raman modes with the highest pressure coefficients. Other modes with large pressure coefficients are the E_g^3 , A_g^3 , and F_g^{12} modes. On the contrary, the two Raman modes with the lowest wavenumber (F_g^1 and F_g^2) are always among the Raman modes with the smallest pressure coefficients, which in some cases can be negative, like in C-type Tb_2O_3 .

The negligible or even negative pressure coefficient of the lowest wavenumber modes of C-type Tb_2O_3 is similar to that observed in other C-type sesquioxides (see Tables 3, S3, and S4). This behavior is also observed in many materials with cubic structures or derived from them, like zincblende or wurtzite compounds, such as ZnO ¹²⁸ or AlN ,¹²⁹ and AB_2X_4 chalcogenides.^{130,131} It has also been observed in zircon-type ABO_4 compounds.^{132,133} Certainly, this anomalous decrease of the wavenumber at HP cannot be explained by an increase of the cation–anion distances at HP, and it could be related to an HP instability of these structures derived from the cubic lattice that show negative pressure coefficients of vibrational modes at the Brillouin zone edge.¹³⁴ In more complex materials (with lower symmetry or with a large number of formula units per primitive cell), these vibrations become Raman or IR-active due to the folding of some Brillouin zone edges into the Brillouin zone center (Γ point). This seems to occur in C-type RE SOs and bixbyite-type SOs.

In regard to the lattice dynamics of B- and A-type SOs, there are several works in which a comparison between their Raman-

mode wavenumbers at room pressure is reported.^{115,123,135,136}

In fact, vibrational modes of both phases are correlated due to the similarity of both B-type and A-type structures, as commented in ref 115. However, we do not know any study in which the pressure coefficients of their Raman-active mode wavenumbers have been compared. A characteristic feature of B-type SOs is that their vibrational spectra can be divided into four regions: (i) the low-wavenumber region below 125 cm^{-1} ; (ii) the medium-low-wavenumber region between 125 and 250 cm^{-1} ; (iii) the medium-high-wavenumber region between 250 and 300 cm^{-1} ; (iv) the high-wavenumber region above 300 cm^{-1} . Among all these spectral regions, only a small phonon gap seems to be visible between the medium-high- and high-wavenumber regions. In Tb_2O_3 , two additional gaps are observed between 450 and 490 cm^{-1} and between 500 and 570 cm^{-1} . The modes in the whole medium-wavenumber region are generally bending Ln–O modes, while those in the high-wavenumber region are generally stretching Ln–O modes. Therefore, we can observe similar trends to those observed for C-type SOs.

In general, the Raman-active mode wavenumbers of B-type SOs increase with an increase in the atomic number, i.e., with a decrease in the unit-cell volume. This result means that, despite Lu having larger mass than Tb, most modes of B-type Lu_2O_3 are observed at higher wavenumbers than those of B-type Tb_2O_3 due to the dominance of the lanthanide contraction effect over the cation mass. The largest difference in wavenumber due to the lanthanide contraction effect is observed in the high-wavenumber modes. These modes are mainly related to O vibrations, so the cation mass is not the dominant factor. On the contrary, both effects get balanced in the low-wavenumber region, where the vibrational modes have a larger contribution of cations. This explains the similar frequencies of B_g^1 , A_g^1 , B_g^2 , and A_g^2 modes along the Sm to Lu series (see Table S5). As for C-type SOs, the theoretical pressure coefficients of the vibrational modes of B-type SOs tend to increase with increasing wavenumber. This means that the smallest pressure coefficients are observed in the low-wavenumber region, while the largest pressure coefficients are found in the medium- and high-wavenumber regions. In particular, the two largest pressure coefficients have been found for the medium-wavenumber modes A_g^8 and B_g^4 followed by the three highest-wavenumber modes (A_g^{12} , A_g^{13} , and A_g^{14}). On the contrary, the two Raman modes with the lowest wavenumber (B_g^1 and A_g^2) are always among the Raman modes with the smallest pressure coefficients, with the B_g^3 , A_g^4 , and A_g^7 modes also being among the ones with the lowest pressure coefficients. In particular, the one for the A_g^7 mode is negative in Tb_2O_3 .

The characteristic phonon modes of A-type SOs have been studied and compared for several SOs.^{115,123,126,127,135,136} A distinctive feature of A-type SOs is that they exhibit a phonon gap between the two lowest wavenumber modes, i.e., the two bending E_g^1 and A_{1g}^1 modes, and also between the two lowest and the two highest wavenumber modes, i.e., the stretching A_{1g}^2 and E_g^2 modes. In fact, the two stretching modes of A-type SOs have been shown to correspond to two different Ln–O(II) bond distances. As in the case of B-type SOs, we observe similar trends in A-type SOs to those observed in the C-type phase. From Table S7, we can see that the two stretching Raman-active mode wavenumbers at 0 GPa of A-type SOs tend to increase with an increase in the atomic number, i.e., with a decrease in the unit-cell volume. In this way, the two

stretching Raman-active modes of A-type Tb_2O_3 (extrapolated at 0 GPa) have a higher wavenumber than those of A-type La_2O_3 despite La having smaller mass than Tb. The same occurs for Sm_2O_3 and Y_2O_3 . This is in agreement with the correlation found between the zero-pressure wavenumbers of the two stretching Raman modes and the c/a ratios of the hexagonal unit cell. Note that c/a values around 1.577 (1.617) are expected for A-type Tb_2O_3 (Y_2O_3) at 0 GPa.⁷⁹ This result shows the dominance of the lanthanide contraction effect over the cation mass in the stretching modes. Again, the largest difference in wavenumber due to the lanthanide contraction effect is observed in the high-wavenumber modes, and the smallest difference is observed in the low-wavenumber modes, where both effects (cation mass and unit-cell contraction) get balanced (see Table S7).

It must be stressed that there is an increasing difference between the wavenumbers of the two stretching modes, $\Delta\omega$, of A-type SOs at 0 GPa as the atomic number increases or the unit-cell volume decreases (see Table S7). Curiously, A-type Y_2O_3 does not seem to follow the trend observed for the rest of A-type SOs. This has prompted us to think about the linear relationship between the c/a ratio and the wavenumbers of the two stretching modes in A-type RE SOs (see Figure 15). Our

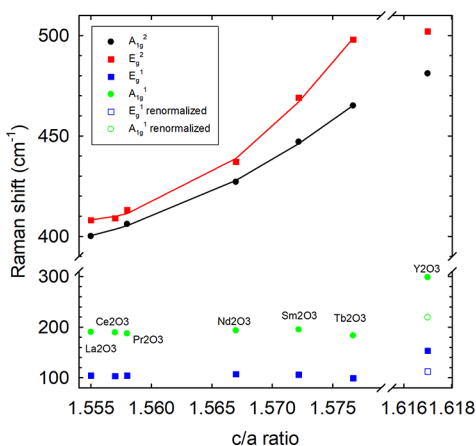


Figure 15. Dependence of the experimental Raman-mode frequencies in A-type SOs with the c/a ratio. Data have been taken from Table S7. Renormalized frequency data for Y_2O_3 have been calculated as commented in the main text.

extrapolated data of the two stretching mode wavenumbers for A-type Tb_2O_3 and A-type Y_2O_3 at room pressure suggest that there is a quadratic trend for A-type RE SOs instead of a linear trend as previously assumed.^{115,123,135} Moreover, we can conclude that the relationship seems to be valid for RE SOs, but it does not apply for Y_2O_3 nor probably for Sc_2O_3 .

In a similar way, the comparable wavenumbers of the two bending modes of A-type RE SOs along the whole RE series also break for Y_2O_3 . However, this disagreement can be solved if we consider that the two low-wavenumber modes of A-type SOs, whose wavenumbers are usually below 200 cm^{-1} , are related to cation vibrations (see Figure S13), as in C-type SOs, and therefore, they are strongly influenced by the cation mass. In such a case, we can renormalize the wavenumbers of Y_2O_3 by multiplying the real wavenumbers of Y_2O_3 by $\sqrt{m_{\text{Y}}/m_{\text{Ho}}}$ (which equals 0.7342) since the ionic radii of Y and Ho are very similar.¹²¹ After the renormalization, we find that the renormalized wavenumbers of Y_2O_3 fall in the region of other

RE SOs (see Figure 15). Therefore, we can conclude that this result indicates that the two low-wavenumber modes of A-type SOs are strongly influenced by cation vibrations. Note that, given the similar atomic mass of Ln atoms relative to Y, similar conclusions would have been obtained by employing other Ln atoms instead of Ho. On the other hand, a similar renormalization can be performed for the high-wavenumber modes if we multiply by $\sqrt{\mu_{\text{Y}}/\mu_{\text{Ho}}}$ (which equals 0.9642), where μ_{X} is the reduced mass of X and O atoms. In such a case, no drastic change in wavenumbers is observed for Y_2O_3 , thus supporting the conclusion that no correlation exists between the high-wavenumber stretching modes of Y_2O_3 and the c/a ratio of the A-type structure of RE SOs.

The above conclusions regarding the nature of the Raman-active modes of A-type SOs are supported by our *ab initio* calculations of A-type Tb_2O_3 at 0 GPa (see Table S7). It can be observed that there is a good agreement between our theoretical and extrapolated experimental low-wavenumber Raman-active mode wavenumbers at 0 GPa. On the other hand, the high-wavenumber Raman-active modes show a difference of 2–3% that could be related to the fact that the pressure coefficients of these vibrational modes could tend to decrease as pressure increases, thus rendering a not so good extrapolation of experimental modes to 0 GPa. In other words, the experimental pressure coefficients obtained for the high-wavenumber modes of A-type Tb_2O_3 at 11 GPa and listed in Table S6 are likely smaller than those at 0 GPa. This is consistent with the smaller pressure coefficient of the E_g^2 mode in Tb_2O_3 at 11 GPa than those found in Sm_2O_3 , Nd_2O_3 , and La_2O_3 at 0 GPa or close to 0 GPa.

Our calculations have allowed us to represent the atomic vibrations of the Raman-active modes of A-type Tb_2O_3 using the J-ICE software.¹³⁷ We have clearly observed that the classification of the two low-wavenumber and the two high-wavenumber Raman-active modes as pure bending and stretching modes is not correct. First of all, we have to note that there are no pure stretching or pure bending modes. In all vibrations, O(I) atoms are immobile. The low-wavenumber E_g^1 mode corresponds to a mixture of bending and stretching modes where Ln atoms vibrate in the hexagonal a – b plane with a small vibration of the O(II) atoms (see Figure S13a). On the other hand, the low-wavenumber A_{1g}^1 mode corresponds to a mixture of a stretching and bending mode where Ln atoms vibrate along the hexagonal c -axis against the O(II) atoms (see Figure S13b). All modes of Tb_2O_3 below (above) 190 cm^{-1} at 0 GPa (see Table S8) show negligible contribution of the O(II) (Ln) atoms. This result means that vibrational modes of the A-type SOs (and likely also for B-type SOs) show similar patterns to those of C-type SOs, i.e., dominance of Ln (O) vibrations below (above) $\sim 200\text{ cm}^{-1}$. Finally, in regard to the high-wavenumber modes, the A_{1g}^2 mode corresponds to a mixture of a stretching and bending mode where Ln atoms vibrate along the hexagonal c -axis against the O(II) atoms (see Figure S14a). On the other hand, the E_g^2 mode corresponds to a mixture of bending and stretching modes where O(II) atoms vibrate in the hexagonal a – b plane with a small vibration of the Ln atoms (see Figure S14b).

In general and similarly to C- and B-type SOs, the theoretical pressure coefficients of the Raman-active modes of A-type SOs increase with increasing wavenumber, except for the A_{1g}^1 and A_{1g}^2 modes of Nd_2O_3 and La_2O_3 (see Table S6).

In fact, taking into account the values of the pressure coefficients for Sm_2O_3 and Tb_2O_3 , one can find that the two low-wavenumber modes are around 106 and 100 cm^{-1} at 0 GPa for the E_g^1 mode, respectively, and around 195 and 185 cm^{-1} at 0 GPa for the A_{1g}^1 mode, respectively. This result agrees with the previous observation that the two low-wavenumber modes show almost fixed wavenumbers around 105 and 190 cm^{-1} .^{115,123,135} Once again, this trend seems not to be obeyed by A-type Y_2O_3 , whose extrapolated values at 0 GPa for the two low-wavenumber modes are around 150 and 300 cm^{-1} , respectively. This suggests a different behavior of the low-wavenumber modes in A-type Y_2O_3 , and probably also in A-type Sc_2O_3 , from that in other RE SOs, which points to stronger bonding forces in the former two compounds. This different behavior, more particularly in the case of Y_2O_3 , could be related to the slightly lower theoretical bulk moduli predicted for these two materials relative to the rest of the RE SOs (see theoretical values in Figure 9b).

In summary, we have provided RS measurements and lattice-dynamics calculations of Tb_2O_3 up to 25 GPa and shown that there is a good agreement between experimental and theoretical wavenumbers for the Raman-active modes of the three phases (C-, B-, and A-type) of Tb_2O_3 . This result confirms the two structural PTs already observed by XRD measurements and supported by total-energy *ab initio* calculations. Since B-type Tb_2O_3 is metastable at room conditions on the downstroke when starting from the B- or the A-type phases, we have provided for the first time the RS spectrum of B-type Tb_2O_3 at room pressure and at HP, which will help future studies to identify this phase by RS measurements instead of resorting to more complex XRD measurements. Besides, we have provided the pressure dependence of the Raman-active modes of A-type Tb_2O_3 from 11 to 25 GPa. On top of that, we have analyzed in detail the nature of the Raman-active modes of A-type Tb_2O_3 in relation to previous works of A-type RE SOs. Finally, we have studied and compared the pressure coefficients of the different Raman-active modes of C-, B-, and A-type RE SOs (including Sc_2O_3 and Y_2O_3) and found a good correlation between the Raman-active modes between the three phases. Notably, we have found that modes below (above) ~ 200 cm^{-1} correspond mainly to vibrations of Ln (O) atoms in all three phases.

5. CONCLUSIONS

We have reported a joint experimental and theoretical study of the structural and vibrational properties of cubic terbium sesquioxide at high pressure. Powder X-ray diffraction and Raman scattering measurements up to 25 GPa show that C-type Tb_2O_3 undergoes two phase transitions: a first irreversible reconstructive transition to the monoclinic B-type phase at ~ 7 GPa and a subsequent reversible displacive transition from the monoclinic to the trigonal A-type phase at ~ 12 GPa. The C \rightarrow B \rightarrow A phase transition sequence observed in Tb_2O_3 is in good agreement with those observed in rare earth sesquioxides crystallizing in the cubic phase at room pressure, as recently reviewed.¹⁵ We speculate that the C–B transition is a strong first-order phase transition (volume collapse around 8%), involving a considerable structural reconstruction. Thus, most likely, there is a kinetic energy barrier, which prevents the system to go back from the B-type structure to the original C-type structure on decreasing pressure, i.e., on decreasing the energy provided to the system. Therefore, the irreversibility of

this transition at room temperature can probably be linked to the kinetic-energy barrier effect, as observed in other compounds, like for instance the zircon–scheelite phase transition in a number of ABO_4 compounds.¹³⁸ On the contrary, the B–A phase transition seems to be a weak first-order phase transition (volume collapse below 2%), and it is a reversible transition at room temperature because it probably implies a much smaller kinetic energy barrier between both structurally-related phases.

We have provided the experimental equation of state for the C-, B-, and A-type phases of Tb_2O_3 . Our results for Tb_2O_3 are in rather good agreement with previous works on other rare earth sesquioxides. Furthermore, our *ab initio* theoretical calculations predict phase transition pressures and bulk moduli for the three phases in rather good agreement with experimental results. Thanks to our calculations, we have discussed the relationship between the unit-cell volume and bulk moduli in C-type/bixbyite, B- and A-type sesquioxides as a function of the atomic number and of the third power of the cation ionic size. The relationship regarding the unit-cell volume has allowed us to check the agreement between the experimental and theoretical results for the three phases in all known sesquioxides. In particular, we have shown that there is a linear trend between the bulk moduli of the three C-, B-, and A-type phases and the cube cation ionic radius. Moreover, we have discussed the ordering of the bulk moduli in the three phases, which seems to be related to the filling of the *f* orbitals.

Raman-active modes of the three phases have been monitored as a function of pressure, and rather good agreement with lattice-dynamics calculations has been found. This agreement has allowed us to confirm the assignment of the experimental phonon modes in the C- and A-type phases as well as to make a tentative assignment of the symmetry of most vibrational modes in the B-type phase. Finally, the Raman-active phonon wavenumbers and their phonon pressure coefficients for the three phases of Tb_2O_3 have been compared with those of other rare earth sesquioxides. In particular, we have shown that the wavenumbers of the high-wavenumber Raman-active modes of A-type sesquioxides do not scale linearly with the *c/a* ratio, as previously assumed, and that the wavenumbers of the high-wavenumber Raman-active modes of A-type Y_2O_3 at room pressure do not seem to scale with those of other rare earth sesquioxides, and the same seems to be valid for Sc_2O_3 . On the other hand, there does not seem to be any relationship between the *c/a* ratio and the wavenumbers of the low-wavenumber Raman-active modes of A-type sesquioxides, which show rather constant values in all compounds.

The present work has been devoted to construct a reference framework to understand the high pressure behavior of the structural and vibrational properties of RE SOs and isostructural compounds. We hope that this study will stimulate further work on different sesquioxides to better constrain their bulk moduli, since some values reported in the literature seem to be quite underestimated or overestimated. We also hope that more work will be carried out on the less well-known A-type phase sesquioxides. In particular, more high pressure studies should be performed for the following compounds: Dy_2O_3 , Ho_2O_3 , Er_2O_3 , Tm_2O_3 , Yb_2O_3 , Lu_2O_3 , and Sc_2O_3 . Such studies would complete the sequence of known A-type sesquioxides and would provide a better understanding of the behavior of this phase under compression.

■ ASSOCIATED CONTENT

SI Supporting Information

The Supporting Information is available free of charge at <https://pubs.acs.org/doi/10.1021/acs.inorgchem.0c00834>.

Whole pattern fittings at different pressures, additional experimental and theoretical structural and vibrational data for C-, A-, and B-type Tb_2O_3 and isostructural compounds, representation of atomic vibrations for selected phonons of Tb_2O_3 , and calculation of the experimental and theoretical compressibility tensor of B-type Tb_2O_3 at different pressures (PDF)

■ AUTHOR INFORMATION

Corresponding Authors

Robert Oliva – Faculty of Fundamental Problems of Technology, Wrocław University of Science and Technology, 50-370 Wrocław, Poland; orcid.org/0000-0002-9378-4048; Email: robert.oliva.vidal@pwr.edu.pl

Francisco Javier Manjón – Instituto de Diseño para la Fabricación y Producción Automatizada, MALTA Consolider Team, Universitat Politècnica de València, 46022 Valencia, Spain; orcid.org/0000-0002-3926-1705; Email: fjmanjon@fis.upv.es

Authors

Jordi Ibáñez – Institute of Earth Sciences Jaume Almera, MALTA Consolider Team, Consell Superior d'Investigacions Científiques (CSIC), 08028 Barcelona, Catalonia, Spain

Juan Ángel Sans – Instituto de Diseño para la Fabricación y Producción Automatizada, MALTA Consolider Team, Universitat Politècnica de València, 46022 Valencia, Spain; orcid.org/0000-0001-9047-3992

Vanessa Cuenca-Gotor – Instituto de Diseño para la Fabricación y Producción Automatizada, MALTA Consolider Team, Universitat Politècnica de València, 46022 Valencia, Spain; orcid.org/0000-0003-0819-8528

Óscar Gomis – MALTA Consolider Team, Universitat Politècnica de València, 46022 Valencia, Spain; orcid.org/0000-0001-6763-0638

Plácida Rodríguez-Hernández – Departamento de Física, Instituto de Materiales y Nanotecnología, MALTA Consolider Team, Universidad de La Laguna, 38200 San Cristóbal de la Laguna, Tenerife, Spain; orcid.org/0000-0002-4148-6516

Alfonso Muñoz – Departamento de Física, Instituto de Materiales y Nanotecnología, MALTA Consolider Team, Universidad de La Laguna, 38200 San Cristóbal de la Laguna, Tenerife, Spain; orcid.org/0000-0003-3347-6518

Ulises Rodríguez-Mendoza – Departamento de Física, Instituto de Materiales y Nanotecnología, MALTA Consolider Team, Universidad de La Laguna, 38200 San Cristóbal de la Laguna, Tenerife, Spain

Matías Velázquez – University of Grenoble Alpes, CNRS, Grenoble INP, SIMAP, 38000 Grenoble, France

Philippe Veber – CNRS, Institut Lumière Matière, Université Claude Bernard Lyon 1, UMR5306, 69622 Villeurbanne, France; orcid.org/0000-0002-0204-1266

Catalin Popescu – ALBA-CELLS, MALTA Consolider Team, 08290 Cerdanyola del Vallès (Barcelona), Catalonia, Spain

Complete contact information is available at: <https://pubs.acs.org/doi/10.1021/acs.inorgchem.0c00834>

Author Contributions

F.J.M. and J.I. prompted the investigation and wrote the manuscript with contributions from the rest of the authors. J.A.S., V.C.-G., and F.J.M. performed the HP-XRD measurements, assisted by C.P. at ALBA synchrotron. J.A.S. and V.C.-G. analyzed the XRD results. J.I. and J.A.S. performed the HP-Raman measurements, and J.I. and R.O. analyzed the data. M.V. and P.V. grew the samples used in this work. P.R.-H. and A.M. performed all the DFT calculations. Finally, O.G. performed the calculations of compressibility tensors, and U.R.-M. contributed to the general discussion of the results.

Notes

The authors declare no competing financial interest.

■ ACKNOWLEDGMENTS

The authors are thankful for the financial support of Generalitat Valenciana under Project PROMETEO 2018/123-EFIMAT and of the Spanish Ministerio de Economía y Competitividad under Projects MAT2015-71035-R, MAT2016-75586-C4-2/3/4-P, and FIS2017-2017-83295-P as well as MALTA Consolider Team research network under project RED2018-102612-T. J.A.S. also acknowledges the Ramón y Cajal program for funding support through RYC-2015-17482. A.M. and P.R.-H. acknowledge computing time provided by Red Española de Supercomputación (RES) and the MALTA Consolider Team cluster. HP-XRD experiments were performed at MPSD beamline of Alba Synchrotron (experiment no. 2016071772). We would like to thank Oriol Blázquez (Universitat de Barcelona) for his contribution to the Raman measurements.

■ REFERENCES

- (1) Pan, T. M.; Chen, F. H.; Jung, J. S. Structural and Electrical Characteristics of High-k Tb_2O_3 and Tb_2TiO_5 Charge Trapping Layers for Nonvolatile Memory Applications. *J. Appl. Phys.* **2010**, *108* (7), 074501.
- (2) Kao, C. H.; Liu, K. C.; Lee, M. H.; Cheng, S. N.; Huang, C. H.; Lin, W. K. High Dielectric Constant Terbium Oxide (Tb_2O_3) Dielectric Deposited on Strained-Si:C. *Thin Solid Films* **2012**, *520*, 3402–3405.
- (3) Gray, N. W.; Prestgard, M. C.; Tiwari, A. Tb_2O_3 Thin Films: An Alternative Candidate for High-k Dielectric Applications. *Appl. Phys. Lett.* **2014**, *105* (22), 222903.
- (4) Geppert, I.; Eizenberg, M.; Bojarczuk, N. A.; Edge, L. F.; Copel, M.; Guha, S. Determination of Band Offsets, Chemical Bonding, and Microstructure of the $(Tb_xSc_{1-x})_2O_3/Si$ System. *J. Appl. Phys.* **2010**, *108* (2), 024105.
- (5) Belaya, S. V.; Bakovets, V. V.; Boronin, A. I.; Koshcheev, S. V.; Lobzareva, M. N.; Korolkov, I. V.; Stabnikov, P. A. Terbium Oxide Films Grown by Chemical Vapor Deposition from Terbium(III) Dipivaloyl methane. *Inorg. Mater.* **2014**, *50* (4), 379–386.
- (6) Bakovets, V. V.; Belaya, S. V.; Lobzareva, M. N.; Maksimovskii, E. A. Kinetics of Terbium Oxide Film Growth from $Tb(Dpm)_3$ Vapor. *Inorg. Mater.* **2014**, *50* (6), 576–581.
- (7) Foex, M.; Traverse, J. P. Investigations about Crystalline Transformation in Rare Earths Sesquioxides at High Temperatures. *Rev. Int. Hautes Temp. Refract.* **1966**, *3* (4), 429–453.
- (8) Zinkevich, M. Thermodynamics of Rare Earth Sesquioxides. *Prog. Mater. Sci.* **2007**, *52* (4), 597–647.
- (9) Warshaw, I.; Roy, R. Polymorphism of the Rare Earth Sesquioxides. *J. Phys. Chem.* **1961**, *65* (11), 2048–2051.
- (10) Brauer, G.; Pfeiffer, B. Mischphasen Aus Praseodym(III)-Oxid Und Terbium(III)-Oxid. *Z. Anorg. Allg. Chem.* **1965**, *341* (5–6), 237–243.

- (11) Tresvyatkii, S. G.; Lopato, L. M.; Schwetschenko, A. W.; Untersuchung Des, K. A. E. Einflusses Hochschmelzender Oxide Der Elemente II. Gruppe Des Periodischen Systems. Auf Polymorphe Hochtem-Peratur-Umwandlungen von Oxiden Der Seltenerdelemente. *Colloq Intern Cent. Natl. Rech Sci. Paris* **1971**, *205*, 247–253.
- (12) Shevthenko, A.V.; Lopato, L.M. TA Method Application to the Highest Refractory Oxide Systems Investigation. *Thermochim. Acta* **1985**, *93*, 537–540.
- (13) Hoekstra, H. R.; Gingerich, K. A. High-Pressure B-Type Polymorphs of Some Rare-Earth Sesquioxides. *Science (Washington, DC, U. S.)* **1964**, *146* (3648), 1163–1164.
- (14) Sawyer, J. O.; Hyde, B. G.; Eyring, L. Pressure and Polymorphism in the Rare Earth Sesquioxides. *Inorg. Chem.* **1965**, *4* (3), 426–427.
- (15) Manjón, F. J.; Sans, J. A.; Ibáñez, J.; Pereira, A. L. J. Pressure-Induced Phase Transitions in Sesquioxides. *Crystals* **2019**, *9* (12), 630.
- (16) Jiang, S.; Liu, J.; Lin, C.; Bai, L.; Xiao, W.; Zhang, Y.; Zhang, D.; Li, X.; Li, Y.; Tang, L. Pressure-Induced Phase Transition in Cubic Lu₂O₃. *J. Appl. Phys.* **2010**, *108* (8), 083541.
- (17) Lin, C. M.; Wu, K.; Hung, T. L.; Sheu, H. S.; Tsai, M. H.; Lee, J. F.; Lee, J. J. Phase Transitions in Lu₂O₃ under High Pressure. *Solid State Commun.* **2010**, *150* (33–34), 1564–1569.
- (18) Meyer, C.; Sanchez, J. P.; Thomasson, J.; Itié, J. P. Mössbauer and Energy-Dispersive x-Ray-Diffraction Studies of the Pressure-Induced Crystallographic Phase Transition in C-Type Yb₂O₃. *Phys. Rev. B: Condens. Matter Mater. Phys.* **1995**, *51* (18), 12187–12193.
- (19) Pandey, S. D.; Samanta, K.; Singh, J.; Sharma, N. D.; Bandyopadhyay, A. K. Anharmonic Behavior and Structural Phase Transition in Y₂O₃. *AIP Adv.* **2013**, *3* (12), 122123.
- (20) Sahu, P. C.; Lonappan, D.; Shekar, N. V. C. High Pressure Structural Studies on Rare-Earth Sesquioxides. *J. Phys. Conf. Ser.* **2012**, *377* (1), 012015.
- (21) Irshad, K. A.; Anees, P.; Sahoo, S.; Sanjay Kumar, N. R.; Srihari, V.; Kalavathi, S.; Chandra Shekar, N. V. Pressure Induced Structural Phase Transition in Rare Earth Sesquioxide Tm₂O₃: Experiment and Ab Initio Calculations. *J. Appl. Phys.* **2018**, *124* (15), 155901.
- (22) Yan, D.; Wu, P.; Zhang, S. P.; Liang, L.; Yang, F.; Pei, Y. L.; Chen, S. Assignments of the Raman Modes of Monoclinic Erbium Oxide. *J. Appl. Phys.* **2013**, *114* (19), 193502.
- (23) Ren, X.; Yan, X.; Yu, Z.; Li, W.; Wang, L. Photoluminescence and Phase Transition in Er₂O₃ under High Pressure. *J. Alloys Compd.* **2017**, *725*, 941–945.
- (24) Guo, Q.; Zhao, Y.; Jiang, C.; Mao, W. L.; Wang, Z.; Zhang, J.; Wang, Y. Pressure-Induced Cubic to Monoclinic Phase Transformation in Erbium Sesquioxide Er₂O₃. *Inorg. Chem.* **2007**, *46* (15), 6164–6169.
- (25) Lonappan, D.; Shekar, N. V. C.; Ravindran, T. R.; Sahu, P. C. High-Pressure Phase Transition in Ho₂O₃. *Mater. Chem. Phys.* **2010**, *120* (1), 65–67.
- (26) Jiang, S.; Liu, J.; Li, X.; Bai, L.; Xiao, W.; Zhang, Y.; Lin, C.; Li, Y.; Tang, L. Phase Transformation of Ho₂O₃ at High Pressure. *J. Appl. Phys.* **2011**, *110* (1), 013526.
- (27) Pandey, S. D.; Samanta, K.; Singh, J.; Sharma, N. D.; Bandyopadhyay, A. K. Raman Scattering of Rare Earth Sesquioxide Ho₂O₃: A Pressure and Temperature Dependent Study. *J. Appl. Phys.* **2014**, *116* (13), 133504.
- (28) Yan, X.; Ren, X.; He, D.; Chen, B.; Yang, W. Mechanical Behaviors and Phase Transition of Ho₂O₃ Nanocrystals under High Pressure. *J. Appl. Phys.* **2014**, *116* (3), 033507.
- (29) Sharma, N. D.; Singh, J.; Dogra, S.; Varandani, D.; Poswal, H. K.; Sharma, S. M.; Bandyopadhyay, A. K. Pressure-Induced Anomalous Phase Transformation in Nano-Crystalline Dysprosium Sesquioxide. *J. Raman Spectrosc.* **2011**, *42* (3), 438–444.
- (30) Jiang, S.; Liu, J.; Lin, C.; Bai, L.; Zhang, Y.; Li, X.; Li, Y.; Tang, L.; Wang, H. Structural Transformations in Cubic Dy₂O₃ at High Pressures. *Solid State Commun.* **2013**, *169*, 37–41.
- (31) Chen, H.; He, C.; Gao, C.; Ma, Y.; Zhang, J.; Wang, X.; Gao, S.; Li, D.; Kan, S.; Zou, G. The Structural Transition of Gd₂O₃ Nanoparticles Induced by High Pressure. *J. Phys.: Condens. Matter* **2007**, *19* (42), 425229.
- (32) Chen, H. Y.; He, C. Y.; Gao, C. X.; Zhang, J. H.; Gao, S. Y.; Lu, H. L.; Nie, Y. G.; Li, D. M.; Kan, S. H.; Zou, G. T. Structural Transition of Gd₂O₃:Eu Induced by High Pressure. *Chin. Phys. Lett.* **2007**, *24* (1), 158–160.
- (33) Zhang, F. X.; Lang, M.; Wang, J. W.; Becker, U.; Ewing, R. C. Structural Phase Transitions of Cubic Gd₂O₃ at High Pressures. *Phys. Rev. B: Condens. Matter Mater. Phys.* **2008**, *78* (6), 064114.
- (34) Dilawar, N.; Varandani, D.; Mehrotra, S.; Poswal, H. K.; Sharma, S. M.; Bandyopadhyay, A. K. Anomalous High Pressure Behaviour in Nanosized Rare Earth Sesquioxides. *Nanotechnology* **2008**, *19* (11), 115703.
- (35) Bai, L.; Liu, J.; Li, X.; Jiang, S.; Xiao, W.; Li, Y.; Tang, L.; Zhang, Y.; Zhang, D. Pressure-Induced Phase Transformations in Cubic Gd₂O₃. *J. Appl. Phys.* **2009**, *106* (7), 073507.
- (36) Zou, X.; Gong, C.; Liu, B.; Li, Q.; Li, Z.; Liu, B.; Liu, R.; Liu, J.; Chen, Z.; Zou, B.; Cui, T.; Bai, X.; Song, H. X-Ray Diffraction of Cubic Gd₂O₃/Er under High Pressure. *Phys. Status Solidi B* **2011**, *248* (5), 1123–1127.
- (37) Zhang, C. C.; Zhang, Z. M.; Dai, R. C.; Wang, Z. P.; Ding, Z. J. High Pressure Luminescence and Raman Studies on the Phase Transition of Gd₂O₃:Eu³⁺ Nanorods. *J. Nanosci. Nanotechnol.* **2011**, *11* (11), 9887–9891.
- (38) Yang, X.; Li, Q.; Liu, Z.; Bai, X.; Song, H.; Yao, M.; Liu, B.; Liu, R.; Gong, C.; Lu, S.; Yao, Z.; Li, D.; Liu, J.; Chen, Z.; Zou, B.; Cui, T.; Liu, B. Pressure-Induced Amorphization in Gd₂O₃/Er³⁺ Nanorods. *J. Phys. Chem. C* **2013**, *117* (16), 8503–8508.
- (39) Chen, G.; Haire, R. G.; Peterson, J. R. Effect of Pressure on Cubic (c-Type) Eu₂O₃ Studied via Eu³⁺ Luminescence. *High Pressure Res.* **1991**, *6* (6), 371–377.
- (40) Chen, G.; Stump, N. A.; Haire, R. G.; Peterson, J. R. Study of the Phase Behavior of Eu₂O₃ under Pressure via Luminescence of Eu³⁺. *J. Alloys Compd.* **1992**, *181* (1–2), 503–509.
- (41) Dilawar, N.; Varandani, D.; Pandey, V. P.; Kumar, M.; Shivaprasad, S. M.; Sharma, P. K.; Bandyopadhyay, A. K. Structural Transition in Nanostructured Eu₂O₃ Under High Pressures. *J. Nanosci. Nanotechnol.* **2006**, *6*, 105–113.
- (42) Sheng, J.; Li-Gang, B.; Jing, L.; Wan-Sheng, X.; Xiao-Dong, L.; Yan-Chun, L.; Ling-Yun, T.; Yu-Feng, Z.; De-Chun, Z.; Li-Rong, Z. The Phase Transition of Eu₂O₃ under High Pressures. *Chin. Phys. Lett.* **2009**, *26* (7), 076101.
- (43) Irshad, K. A.; Chandra Shekar, N. V.; Srihari, V.; Pandey, K. K.; Kalavathi, S. High Pressure Structural Phase Transitions in Ho:Eu₂O₃. *J. Alloys Compd.* **2017**, *725*, 911–915.
- (44) Yu, Z.; Wang, Q.; Ma, Y.; Wang, L. X-Ray Diffraction and Spectroscopy Study of Nano-Eu₂O₃ structural Transformation under High Pressure. *J. Alloys Compd.* **2017**, *701*, 542–548.
- (45) Sheng, J.; Li-Gang, B.; Jing, L.; Wan-Sheng, X.; Xiao-Dong, L.; Yan-Chun, L.; Ling-Yun, T.; Yu-Feng, Z.; De-Chun, Z.; Li-Rong, Z. The Phase Transition of Eu₂O₃ under High Pressures. *Chin. Phys. Lett.* **2009**, *26*, 076101.
- (46) Guo, Q.; Zhao, Y.; Jiang, C.; Mao, W. L.; Wang, Z. Phase Transformation in Sm₂O₃ at High Pressure: In Situ Synchrotron X-Ray Diffraction Study and Ab Initio DFT Calculation. *Solid State Commun.* **2008**, *145* (5–6), 250–254.
- (47) Jiang, S.; Liu, J.; Lin, C.; Li, X.; Li, Y. High-Pressure x-Ray Diffraction and Raman Spectroscopy of Phase Transitions in Sm₂O₃. *J. Appl. Phys.* **2013**, *113* (11), 113502.
- (48) Liu, D.; Lei, W.; Li, Y.; Ma, Y.; Hao, J.; Chen, X.; Jin, Y.; Liu, D.; Yu, S.; Cui, Q.; Zou, G. High-Pressure Structural Transitions of Sc₂O₃ by X-Ray Diffraction, Raman Spectra, and Ab Initio Calculations. *Inorg. Chem.* **2009**, *48* (17), 8251–8256.
- (49) Yusa, H.; Tsuchiya, T.; Sata, N.; Ohishi, Y. High-Pressure Phase Transition to the Gd₂S₃ Structure in Sc₂O₃: A New Trend in Dense Structures in Sesquioxides. *Inorg. Chem.* **2009**, *48* (16), 7537–7543.
- (50) Ovsyannikov, S. V.; Bykova, E.; Bykov, M.; Wenz, M. D.; Pakhomova, A. S.; Glazyrin, K.; Liermann, H. P.; Dubrovinsky, L.

Structural and Vibrational Properties of Single Crystals of Scandia, Sc_2O_3 under High Pressure. *J. Appl. Phys.* **2015**, *118* (16), 165901.

(51) Husson, E.; Proust, C.; Gillet, P.; Itié, J. P. Phase Transitions in Yttrium Oxide at High Pressure Studied by Raman Spectroscopy. *Mater. Res. Bull.* **1999**, *34* (12), 2085–2092.

(52) Bai, X.; Song, H. W.; Liu, B. B.; Hou, Y. Y.; Pan, G. H.; Ren, X. G. Effects of High Pressure on the Luminescent Properties of Nanocrystalline and Bulk $\text{Y}_2\text{O}_3:\text{Eu}^{3+}$. *J. Nanosci. Nanotechnol.* **2008**, *8*, 1404–1409.

(53) Jovanic, B. R.; Dramicanin, M.; Viana, B.; Panic, B.; Radenkovic, B. High-Pressure Optical Studies of $\text{Y}_2\text{O}_3:\text{Eu}^{3+}$ Nanoparticles. *Radiat. Eff. Defects Solids* **2008**, *163* (12), 925–931.

(54) Wang, L.; Pan, Y.; Ding, Y.; Yang, W.; Mao, W. L.; Sinogeikin, S. V.; Meng, Y.; Shen, G.; Mao, H. K. High-Pressure Induced Phase Transitions of Y_2O_3 and $\text{Y}_2\text{O}_3:\text{Eu}^{3+}$. *Appl. Phys. Lett.* **2009**, *94* (6), 061921.

(55) Wang, L.; Yang, W.; Ding, Y.; Ren, Y.; Xiao, S.; Liu, B.; Sinogeikin, S. V.; Meng, Y.; Gosztola, D. J.; Shen, G.; Hemley, R. J.; Mao, W. L.; Mao, H. K. Size-Dependent Amorphization of Nanoscale Y_2O_3 at High Pressure. *Phys. Rev. Lett.* **2010**, *105* (9), 095701.

(56) Halevy, I.; Carmon, R.; Winterrose, M. L.; Yeheskel, O.; Tiferet, E.; Ghose, S. Pressure-Induced Structural Phase Transitions in Y_2O_3 Sesquioxide. *J. Phys. Conf. Ser.* **2010**, *215*, 012003.

(57) Dai, R. C.; Zhang, Z. M.; Zhang, C. C.; Ding, Z. J. Photoluminescence and Raman Studies of $\text{Y}_2\text{O}_3:\text{Eu}^{3+}$ Nanotubes under High Pressure. *J. Nanosci. Nanotechnol.* **2010**, *10* (11), 7629–7633.

(58) Dai, R.; Wang, Z.; Zhang, Z.; Ding, Z. Photoluminescence Study of SiO_2 Coated $\text{Eu}^{3+}:\text{Y}_2\text{O}_3$ Core-Shells under High Pressure. *J. Rare Earths* **2010**, *28* (SUPPL. 1), 241–245.

(59) Yusa, H.; Tsuchiya, T.; Sata, N.; Ohishi, Y. Dense Yttria Phase Eclipsing the A-Type Sesquioxide Structure: High-Pressure Experiments and Ab Initio Calculations. *Inorg. Chem.* **2010**, *49* (10), 4478–4485.

(60) Bose, P. P.; Gupta, M. K.; Mittal, R.; Rols, S.; Achary, S. N.; Tyagi, A. K.; Chaplot, S. L. High Pressure Phase Transitions in Yttria, Y_2O_3 . *J. Phys. Conf. Ser.* **2012**, *377* (1), 012036.

(61) Srivastava, A. M.; Renero-Lecuna, C.; Santamaría-Pérez, D.; Rodríguez, F.; Valiente, R. Pressure-Induced Pr^{3+} - 3P^0 Luminescence in Cubic Y_2O_3 . *J. Lumin.* **2014**, *146*, 27–32.

(62) Yamanaka, T.; Nagai, T.; Okada, T.; Fukuda, T. Structure Change of Mn_2O_3 under High Pressure and Pressure-Induced Transition. *Z. Kristallogr. - Cryst. Mater.* **2005**, *220* (11), 938–945.

(63) Santillán, J.; Shim, S. H.; Shen, G.; Prakapenka, V. B. High-Pressure Phase Transition in Mn_2O_3 : Application for the Crystal Structure and Preferred Orientation of the CaIrO_3 Type. *Geophys. Res. Lett.* **2006**, *33* (15), 2–6.

(64) Shim, S. H.; LaBounty, D.; Duffy, T. S. Raman Spectra of Bixbyite, Mn_2O_3 , up to 40 GPa. *Phys. Chem. Miner.* **2011**, *38* (9), 685–691.

(65) Hong, F.; Yue, B.; Hirao, N.; Liu, Z.; Chen, B. Significant Improvement in Mn_2O_3 Transition Metal Oxide Electrical Conductivity via High Pressure. *Sci. Rep.* **2017**, *7*, 44078.

(66) Yusa, H.; Tsuchiya, T.; Sata, N.; Ohishi, Y. Rh_2O_3 (II) -Type Structures in Ga_2O_3 and In_2O_3 under High Pressure: Experiment and Theory. *Phys. Rev. B - Condens. Matter Mater. Phys.* **2008**, *77* (6), 1–9.

(67) Liu, D.; Lei, W. W.; Zou, B.; Yu, S. D.; Hao, J.; Wang, K.; Liu, B. B.; Cui, Q. L.; Zou, G. T. High-Pressure x-Ray Diffraction and Raman Spectra Study of Indium Oxide. *J. Appl. Phys.* **2008**, *104* (8), 083506.

(68) Qi, J.; Liu, J. F.; He, Y.; Chen, W.; Wang, C. Compression Behavior and Phase Transition of Cubic In_2O_3 Nanocrystals. *J. Appl. Phys.* **2011**, *109* (6), 063520.

(69) García-Domene, B.; Ortiz, H. M.; Gomis, O.; Sans, J. A.; Manjón, F. J.; Muñoz, A.; Rodríguez-Hernández, P.; Achary, S. N.; Errandonea, D.; Martínez-García, D.; Romero, A. H.; Singhal, A.; Tyagi, A. K. High-Pressure Lattice Dynamical Study of Bulk and Nanocrystalline In_2O_3 . *J. Appl. Phys.* **2012**, *112* (12), 123511.

(70) García-Domene, B.; Sans, J. A.; Gomis, O.; Manjón, F. J.; Ortiz, H. M.; Errandonea, D.; Santamaría-Pérez, D.; Martínez-García, D.; Vilaplana, R.; Pereira, A. L. J.; Morales-García, A.; Rodríguez-Hernández, P.; Muñoz, A.; Popescu, C.; Segura, A. PbcA -Type In_2O_3 : The High-Pressure Post-Corundum Phase at Room Temperature. *J. Phys. Chem. C* **2014**, *118* (35), 20545–20552.

(71) Gomis, O.; Santamaría-Pérez, D.; Ruiz-Fuertes, J.; Sans, J. A.; Vilaplana, R.; Ortiz, H. M.; García-Domene, B.; Manjón, F. J.; Errandonea, D.; Rodríguez-Hernández, P.; Muñoz, A.; Mollar, M. High-Pressure Structural and Elastic Properties of Tl_2O_3 . *J. Appl. Phys.* **2014**, *116* (13), 133521.

(72) McClure, J. P. *High Pressure Phase Transitions in the Lanthanide Sesquioxides*. Ph.D. Thesis, University of Nevada, Las Vegas, 2009, pp 1–154.

(73) Hirotsaki, N.; Ogata, S.; Kocer, C. Ab Initio Calculation of the Crystal Structure of the Lanthanide Ln_2O_3 Sesquioxides. *J. Alloys Compd.* **2003**, *351* (1–2), 31–34.

(74) Marsella, L.; Fiorentini, V. Structure and Stability of Rare-Earth and Transition-Metal Oxides. *Phys. Rev. B: Condens. Matter Mater. Phys.* **2004**, *69* (17), 172103.

(75) Petit, L.; Svane, A.; Szotek, Z.; Temmerman, W. M. First-Principles Study of Rare-Earth Oxides. *Phys. Rev. B: Condens. Matter Mater. Phys.* **2005**, *72* (20), 205118.

(76) Wu, B.; Zinkevich, M.; Wang, C.; Aldinger, F. Ab Initio Energetic Study of Oxide Ceramics with Rare-Earth Elements. *Rare Met.* **2006**, *25* (5), 549–555.

(77) Singh, N.; Saini, S. M.; Nautiyal, T.; Auluck, S. Electronic Structure and Optical Properties of Rare Earth Sesquioxides (R_2O_3 , R = La, Pr, and Nd). *J. Appl. Phys.* **2006**, *100* (8), 083525.

(78) Mikami, M.; Nakamura, S. Electronic Structure of Rare-Earth Sesquioxides and Oxysulfides. *J. Alloys Compd.* **2006**, *408–412*, 687–692.

(79) Wu, B.; Zinkevich, M.; Aldinger, F.; Wen, D.; Chen, L. Ab Initio Study on Structure and Phase Transition of A- and B-Type Rare-Earth Sesquioxides Ln_2O_3 (Ln = La-Lu, Y, and Sc) Based on Density Function Theory. *J. Solid State Chem.* **2007**, *180* (11), 3280–3287.

(80) Rahm, M.; Skorodumova, N. V. Phase Stability of the Rare-Earth Sesquioxides under Pressure. *Phys. Rev. B: Condens. Matter Mater. Phys.* **2009**, *80* (10), 104105.

(81) Jiang, H.; Gomez-Abal, R. I.; Rinke, P.; Scheffler, M. Localized and Itinerant States in Lanthanide Oxides United by GW@LDA+U. *Phys. Rev. Lett.* **2009**, *102* (12), 126403.

(82) Gillen, R.; Clark, S. J.; Robertson, J. Nature of the Electronic Band Gap in Lanthanide Oxides. *Phys. Rev. B: Condens. Matter Mater. Phys.* **2013**, *87* (12), 125116.

(83) Richard, D.; Muñoz, E. L.; Rentería, M.; Errico, L. A.; Svane, A.; Christensen, N. E. Abinitio LSDA and LSDA+U Study of Pure and Cd-Doped Cubic Lanthanide Sesquioxides. *Phys. Rev. B: Condens. Matter Mater. Phys.* **2013**, *88* (16), 165206.

(84) Richard, D.; Errico, L. A.; Rentería, M. Structural Properties and the Pressure-Induced C → A Phase Transition of Lanthanide Sesquioxides from DFT and DFT + U Calculations. *J. Alloys Compd.* **2016**, *664*, 580–589.

(85) Ogawa, T.; Otani, N.; Yokoi, T.; Fisher, C. A. J.; Kuwabara, A.; Moriwake, H.; Yoshiya, M.; Kitaoka, S.; Takata, M. Density Functional Study of the Phase Stability and Raman Spectra of Yb_2O_3 , Yb_2SiO_5 and $\text{Yb}_2\text{Si}_2\text{O}_7$ under Pressure. *Phys. Chem. Chem. Phys.* **2018**, *20* (24), 16518–16527.

(86) Pathak, A. K.; Vazhappilly, T. Ab Initio Study on Structure, Elastic, and Mechanical Properties of Lanthanide Sesquioxides. *Phys. Status Solidi B* **2018**, *255* (6), 1700668.

(87) Lonappan, D.; Chandra Shekar, N. V.; Sahu, P. C.; Kumar, J.; Paul, R.; Paul, P. Unusually Large Structural Stability of Terbium Oxide Phase under High Pressure. *J. Alloys Compd.* **2010**, *490* (1–2), 47–49.

(88) Veber, P.; Velázquez, M.; Gadret, G.; Rytz, D.; Peltz, M.; Decourt, R. Flux Growth at 1230 °C of Cubic Tb_2O_3 Single Crystals

and Characterization of Their Optical and Magnetic Properties. *CrystEngComm* **2015**, *17* (3), 492–497.

(89) Ibáñez, J.; Blázquez, O.; Hernández, S.; Garrido, B.; Rodríguez-Hernández, P.; Muñoz, A.; Velázquez, M.; Veber, P.; Manjón, F. J. Lattice Dynamics Study of Cubic Tb₂O₃. *J. Raman Spectrosc.* **2018**, *49* (12), 2021–2027.

(90) McCarthy, G. J. Crystal Data on C-Type Terbium Sesquioxide (Tb₂O₃). *J. Appl. Crystallogr.* **1971**, *4*, 399–400.

(91) Fauth, F.; Peral, I.; Popescu, C.; Knapp, M. The New Material Science Powder Diffraction Beamline at ALBA Synchrotron. In *Powder Diffraction*; Cambridge University Press, 2013; Vol. 28, pp S360–S370.

(92) Dewaele, A.; Loubeyre, P.; Mezouar, M. Equations of State of Six Metals above 94 GPa. *Phys. Rev. B: Condens. Matter Mater. Phys.* **2004**, *70* (9), 094112.

(93) Prescher, C.; Prakapenka, V. B. DIOPTAS: A Program for Reduction of Two-Dimensional X-Ray Diffraction Data and Data Exploration. *High Pressure Res.* **2015**, *35* (3), 223–230.

(94) Mao, H. K.; Xu, J.; Bell, P. M. Calibration of the Ruby Pressure Gauge to 800 Kbar under Quasi-Hydrostatic Conditions. *J. Geophys. Res.* **1986**, *91* (B5), 4673.

(95) Hohenberg, P.; Kohn, W. Inhomogeneous Electron Gas. *Phys. Rev.* **1964**, *136*, B864.

(96) Kresse, G.; Furthmüller, J. Efficiency of Ab-Initio Total Energy Calculations for Metals and Semiconductors Using a Plane-Wave Basis Set. *Comput. Mater. Sci.* **1996**, *6* (1), 15–50.

(97) Blöchl, P. E. Projector Augmented-Wave Method. *Phys. Rev. B: Condens. Matter Mater. Phys.* **1994**, *50* (24), 17953–17979.

(98) Kresse, G.; Joubert, D. From Ultrasoft Pseudopotentials to the Projector Augmented-Wave Method. *Phys. Rev. B: Condens. Matter Mater. Phys.* **1999**, *59* (3), 1758–1775.

(99) Perdew, J. P.; Burke, K.; Ernzerhof, M. Generalized Gradient Approximation Made Simple. *Phys. Rev. Lett.* **1996**, *77* (18), 3865–3868.

(100) Perdew, J. P.; Ruzsinszky, A.; Csonka, G. L.; Vydrov, O. A.; Scuseria, G. E.; Constantin, L. A.; Zhou, X.; Burke, K. Restoring the Density-Gradient Expansion for Exchange in Solids and Surfaces. *Phys. Rev. Lett.* **2008**, *100* (13), 136406.

(101) Monkhorst, H. J.; Pack, J. D. Special Points for Brillouin-Zone Integrations. *Phys. Rev. B* **1976**, *13* (12), 5188–5192.

(102) Parlinski, K. *Phonon Code*; <http://wolf.ifj.edu.pl/phonon/>.

(103) Vegas, A.; Isea, R. Distribution of the M-M Distances in the Rare Earth Oxides. *Acta Crystallogr., Sect. B: Struct. Sci.* **1998**, *54* (6), 732–740.

(104) Vegas, A.; Martin, R. L.; Bevan, D. J. M. Compounds with a Stuffed Anti-Bixbyite-Type Structure, Analysed in Terms of the Zintl-Klemm and Coordination-Defect Concepts. *Acta Crystallogr., Sect. B: Struct. Sci.* **2009**, *65* (1), 11–21.

(105) Porotnikov, N. V.; Kondratov, O. I.; Petrov, K. I. Calculation of Theoretical Vibration Spectra of RE Oxides of C-Type: Lu₂O₃, Gd₂O₃, Sc₂O₃. *Russ. J. Inorg. Chem.* **1985**, *30*, 931.

(106) Klotz, S.; Chervin, J.-C.; Munsch, P.; Le Marchand, G. Hydrostatic Limits of 11 Pressure Transmitting Media. *J. Phys. D: Appl. Phys.* **2009**, *42* (7), 075413.

(107) Hoekstra, H. R. Phase Relationships in the Rare Earth Sesquioxides at High Pressure. *Inorg. Chem.* **1966**, *5* (5), 754–757.

(108) Hubbert-Paletta, E.; Müller-Buschbau, H. Röntgenographische Untersuchung an Einkristallen von Monoklinem Tb₂O₃. *Z. Anorg. Allg. Chem.* **1968**, *363* (3–4), 145–150.

(109) Adachi, G. Y.; Imanaka, N. The Binary Rare Earth Oxides. *Chem. Rev.* **1998**, *98* (4), 1479–1514.

(110) Birch, F. The Effect of Pressure upon the Elastic Parameters of Isotropic Solids, According to Murnaghan's Theory of Finite Strain. *J. Appl. Phys.* **1938**, *9* (4), 279–288.

(111) Vegas, A. Structural Models of Inorganic Crystals. In *Structural Models of Inorganic Crystals*; Universitat Politècnica de València: Valencia, 2018; pp 105–106.

(112) Spedding, F. H.; Hanak, J. J.; Daane, A. H. High temperature allotropy and thermal expansion of the rare-earth metals. *J. Less-Common Met.* **1961**, *3* (2), 110–124.

(113) Chen, G.; Peterson, J. R.; Brister, K. E. An Energy-Dispersive X-Ray Diffraction Study of Monoclinic Eu₂O₃ under Pressure. *J. Solid State Chem.* **1994**, *111*, 437–439.

(114) Zhang, Q.; Wu, X.; Qin, S. Pressure-Induced Phase Transition of B-Type Y₂O₃. *Chin. Phys. B* **2017**, *26*, 090703.

(115) Gouteron, J.; Michel, D.; Lejus, A. M.; Zarembowitch, J. Raman Spectra of Lanthanide Sesquioxide Single Crystals: Correlation between A and B-Type Structures. *J. Solid State Chem.* **1981**, *38* (3), 288–296.

(116) Lipp, M. J.; Jeffries, J. R.; Cynn, H.; Park Klepeis, J. H.; Evans, W. J.; Mortensen, D. R.; Seidler, G. T.; Xiao, Y.; Chow, P. Comparison of the High-Pressure Behavior of the Cerium Oxides Ce₂O₃ and CeO₂. *Phys. Rev. B: Condens. Matter Mater. Phys.* **2016**, *93* (6), 064106.

(117) Pandey, K. K.; Garg, N.; Mishra, A. K.; Sharma, S. M. High Pressure Phase Transition in Nd₂O₃. *J. Phys. Conf. Ser.* **2012**, *377* (1), 012006.

(118) Zhang, Q.; Yang, J.; Wu, X.; Qin, S. Phase Stability and Elasticity of Sc₂O₃ at High Pressure. *Eur. Phys. J. B* **2011**, *84* (1), 11–16.

(119) Shannon, R. D. Revised Effective Ionic Radii and Systematic Studies of Interatomic Distances in Halides and Chalcogenides. *Acta Crystallogr., Sect. A: Cryst. Phys., Diffr., Theor. Gen. Crystallogr.* **1976**, *32* (5), 751–767.

(120) Shannon, R. D.; Prewitt, C. T. Synthesis and Structure of a New High-Pressure Form of Rh₂O₃. *J. Solid State Chem.* **1970**, *2* (1), 134–136.

(121) Danno, T.; Nakatsuka, D.; Kusano, Y.; Asaoka, H.; Nakanishi, M.; Fujii, T.; Ikeda, Y.; Takada, J. Crystal Structure of β-Fe₂O₃ and Topotactic Phase Transformation to α-Fe₂O₃. *Cryst. Growth Des.* **2013**, *13* (2), 770–774.

(122) Abrashev, M. V.; Todorov, N. D.; Geshev, J. Raman Spectra of R₂O₃ (R - Rare Earth) Sesquioxides with C-Type Bixbyite Crystal Structure: A Comparative Study. *J. Appl. Phys.* **2014**, *116*, 103508.

(123) Zarembowitch, J.; Gouteron, J.; Lejus, A. M. Raman Spectra of Lanthanide Sesquioxide Single Crystals with A-Type Structure. *Phys. Status Solidi B* **1979**, *94* (1), 249–256.

(124) Zarembowitch, J.; Gouteron, J.; Lejus, A. M. Raman Spectrum of Single Crystals of Monoclinic B-Type Gadolinium Sesquioxide. *J. Raman Spectrosc.* **1980**, *9* (4), 263–265.

(125) Aldebert, P.; Traverse, J. P. Etude Par Diffraction Neutronique Des Structures de Haute Temperature de La₂O₃ et Nd₂O₃. *Mater. Res. Bull.* **1979**, *14* (3), 303–323.

(126) Hongo, T.; Kondo, K. I.; Nakamura, K. G.; Atou, T. High Pressure Raman Spectroscopic Study of Structural Phase Transition in Samarium Oxide. *J. Mater. Sci.* **2007**, *42* (8), 2582–2585.

(127) Jiang, S.; Liu, J.; Bai, L.; Li, X.; Li, Y.; He, S.; Yan, S.; Liang, D. Anomalous Compression Behaviour in Nd₂O₃ Studied by X-Ray Diffraction and Raman Spectroscopy. *AIP Adv.* **2018**, *8* (2), 025019.

(128) Manjón, F. J.; Syassen, K.; Lauck, R. Effect of Pressure on Phonon Modes in Wurtzite Zinc Oxide. *High Pressure Res.* **2002**, *22* (2), 299–304.

(129) Manjón, F. J.; Errandonea, D.; Romero, A. H.; Garro, N.; Serrano, J.; Kuball, M. Lattice Dynamics of Wurtzite and Rocksalt AlN under High Pressure: Effect of Compression on the Crystal Anisotropy of Wurtzite-Type Semiconductors. *Phys. Rev. B: Condens. Matter Mater. Phys.* **2008**, *77* (20), 205204.

(130) Gomis, O.; Vilaplana, R.; Manjón, F. J.; Pérez-González, E.; López-Solano, J.; Rodríguez-Hernández, P.; Muñoz, A.; Errandonea, D.; Ruiz-Fuertes, J.; Segura, A.; Santamara-Pérez, D.; Tiginyanu, I. M.; Ursaki, V. V. High-Pressure Optical and Vibrational Properties of CdGa₂Se₄: Order-Disorder Processes in Adamantine Compounds. *J. Appl. Phys.* **2012**, *111* (1), 013518.

(131) Vilaplana, R.; Robledillo, M.; Gomis, O.; Sans, J. A.; Manjón, F. J.; Pérez-González, E.; Rodríguez-Hernández, P.; Muñoz, A.;

Tiginyanu, I. M.; Ursaki, V. V. Vibrational Study of HgGa_2S_4 under High Pressure. *J. Appl. Phys.* **2013**, *113* (9), 093512.

(132) Manjón, F. J.; Rodríguez-Hernández, P.; Muñoz, A.; Romero, A. H.; Errandonea, D.; Syassen, K. Lattice Dynamics of YVO_4 at High Pressures. *Phys. Rev. B: Condens. Matter Mater. Phys.* **2010**, *81* (7), 075202.

(133) Panchal, V.; Manjón, F. J.; Errandonea, D.; Rodríguez-Hernández, P.; López-Solano, J.; Muñoz, A.; Achary, S. N.; Tyagi, A. K. High-Pressure Study of ScVO_4 by Raman Scattering and Ab Initio Calculations. *Phys. Rev. B: Condens. Matter Mater. Phys.* **2011**, *83* (6), 064111.

(134) Weinstein, B. A.; Zallen, R. *Light Scattering in Solids*; Cardona, M., Güntherodt, G., Eds.; Springer: Berlin, 1984; Vol. IV.

(135) Avisar, D.; Livneh, T. The Raman-Scattering of A-Type Ce_2O_3 . *Vib. Spectrosc.* **2016**, *86*, 14–16.

(136) Boldish, S. I.; White, W. B. Vibrational Spectra of Crystals with the A-Type Rare Earth Oxide Structure-I. La_2O_3 and Nd_2O_3 . *Spectrochim. Acta Part A Mol. Spectrosc.* **1979**, *35* (11), 1235–1242.

(137) Canepa, P.; Hanson, R. M.; Ugliengo, P.; Alfredsson, M. J-ICE: A New Jmol Interface for Handling and Visualizing Crystallographic and Electronic Properties. *J. Appl. Crystallogr.* **2011**, *44* (1), 225–229.

(138) Errandonea, D.; Manjón, F. J.; Muñoz, A.; Rodríguez-Hernández, P.; Panchal, V.; Achary, S. N.; Tyagi, A. K. High-Pressure Polymorphs of TbVO_4 : A Raman and Ab Initio Study. *J. Alloys Compd.* **2013**, *577*, 327–335.